

THESIS

MAPPING EVAPOTRANSPIRATION AT A HIGH RESOLUTION USING THE SURFACE
AERODYNAMIC TEMPERATURE MODEL AND AIRBORNE MULTISPECTRAL
REMOTE SENSING DATA

Submitted by

Melahat Semin Barlak

Department of Civil and Environmental Engineering

In partial fulfilment of the requirements

For the Degree of Master of Science

Colorado State University

Fort Collins, Colorado

Fall 2016

Master's Committee:

Advisor: José L. Chávez

Allan Andales

Meagan Schipanski

Copyright by Melahat Semin Barlak 2016

All Rights Reserved

ABSTRACT

MAPPING EVAPOTRANSPIRATION AT A HIGH RESOLUTION USING THE SURFACE AERODYNAMIC TEMPERATURE MODEL AND AIRBORNE MULTISPECTRAL REMOTE SENSING DATA

Irrigation is the largest single consumer of water in the world, and with the increasing population, limitation of natural resources, climate change, and global warming, the pressure on water resources has become more significant and attention to agriculture is increasing daily. The limitation of agricultural areas requires efficient use of these areas to obtain a maximum yield. Evapotranspiration (ET) is a major component of the water budget and energy balance. Therefore, exact measurement of plant water use (and thus ET) is vital for efficient use of water resources, planning, and management purposes, especially for arid and semiarid regions. Many methods have been developed for estimating crop ET on a small field scale, such as the Bowen Ratio (BR), the Eddy Covariance (EC), and Lysimeter systems; however, remote sensing-based ET methods have been developed for estimating crop water needs on a regional scale. The energy balance (EB)-based ET algorithms require the computation of net radiation (R_n), soil heat flux (G), and sensible heat flux (H) to solve for latent heat flux or ET as a residual. Values of R_n and G can be estimated with an acceptable accuracy. However, estimation of H is not straightforward. This is because surface aerodynamic temperature (T_o) is difficult to measure or estimate. Instead, radiometric surface temperature (T_s) is generally used in the estimation of H . However, using T_s may cause overestimation of H , and thus underestimation of ET. To account for those differences between T_o and T_s , several remote sensing-based algorithms have been developed for mapping ET. The Surface Aerodynamic Temperature (SAT) model is one of them, and was used in this study to estimate sensible heat flux (H) for cotton fields and calculate ET as

a residual of the EB for research fields located at the USDA-ARS Conservation and Production Research Laboratory (CPRL) near Bushland, Texas in 2008. By using the SAT model, ET results obtained from the multispectral airborne remote sensing data were compared with ET calculated with model input data collected at the large weighing lysimeters site. Resulting SAT ET values were obtained with a Mean Biased error (MBE) and a Root Mean Squared error (RMSE) of 2.67% and 8.61%, respectively. Then, actual crop ET from the SAT model were compared to measured values from the large lysimeter mass balance. This evaluation resulted in 25.9% MBE and a 44.07% RMSE for the east irrigated fields while for the west dryland fields the error obtained was 42.13% MBE and 42.91% RMSE. In addition, the crop water stress index (CWSI) was used to calculate actual ET using remote sensing inputs and results were also compared to lysimeter measured ET values. Results indicated that the errors were MBE value of 3.77% and an RMSE value of 10.76% for the east fields and 0.89% MBE and 6.0% RMSE for the west fields of the research area, respectively. The results show that the SAT model that was used in this study may not be appropriate for sparse vegetation and heterogeneous surface conditions and that further improvement of the model is required with the application of remote sensing data. On the other hand, the CWSI method performed better than the SAT model for estimating ET and crop water stress levels.

ACKNOWLEDGEMENTS

First, I would like to express my sincere gratitude to my advisor, Dr. José L. Chávez, for his continuous support of my study, as well as his patience, motivation, and immense knowledge. His guidance helped me throughout the entire research process and writing of this thesis.

Besides my advisor, I would like to thank the rest of my thesis committee, Dr. Allan Andales and Dr. Meagan Schipanski, for their insightful comments and advice.

I would also like to thank my friends for their continuous support.

A special thanks goes to my amazing family for inspiring me to go after my dreams and for never ceasing to support me. Words cannot express how grateful I am to have you in my life.

TABLE OF CONTENTS

CHAPTER 1: INTRODUCTION.....	1
1.1 Water Scarcity and Drought.....	1
1.2 Population Growth.....	2
1.3 Global Warming and Climate Change.....	2
1.4 Irrigated Agriculture.....	3
1.5 ASCE Standardized Reference ET Equation.....	4
1.6 Crop Evapotranspiration.....	6
1.7 Plant Water Stress.....	7
1.8 Weighing Lysimeters.....	10
1.9 Remote Sensing System.....	10
1.9.1 Remote Sensing Models for Estimating ET.....	14
1.10 The Surface Aerodynamic Temperature (SAT) Model.....	16
1.11 Objectives.....	18
CHAPTER 2: METHODOLOGY.....	19
2.1 Site Description.....	19
2.2 Weighing Lysimeter Data.....	21
2.3 Meteorological Data.....	22
2.4 Remote Sensing Data.....	26
2.5 Calculation of Water Stress.....	33
2.6 Statistical Analysis.....	33
CHAPTER 3: RESULTS AND ANALYSIS.....	35
3.1 rah Estimation.....	38
3.2 To Estimation.....	41
3.3 H estimation.....	44
3.4 Rn Estimation.....	47
3.5 G Estimation.....	49
3.6 ET estimation.....	51
3.7 CWSI Assessment.....	63
CHAPTER 4: CONCLUSION.....	67

REFERENCES	70
APPENDIX A	73
APPENDIX B	78
APPENDIX C	82
APPENDIX D	87

LIST OF TABLES

Table 1. Weather data used for remote sensing calculation.....	23
Table 2. North-east lysimeter weather data	24
Table 3. North-west lysimeter weather data	24
Table 4. South-east lysimeter weather data	25
Table 5. South-west lysimeter weather data	25
Table 6. Calculated rah for lysimeter and remote sensing for the given research areas and dates	41
Table 7. Calculated To values for lysimeter and remote sensing for the given research areas and dates	43
Table 8. Calculated H values for lysimeter and remote sensing for the given research areas and dates	46
Table 9. Calculated Rn values with lysimeter and remote sensing for the given research areas and dates	49
Table 10. Calculated G values with lysimeter and remote sensing for the given research areas and dates	51
Table 11. Lysimeter calculated rah, To, H, Rn, G, and ETa values for the given research areas and dates.....	60
Table 12. Remote Sensing obtained rah, To, H, Rn, G and ET values for the given research areas and dates.....	61
Table 13. Daily ET values obtained from the lysimeter and remote sensing methods.....	62
Table 14. Obtained CWSI values with lysimeter and remote sensing calculations for east part of the research area.....	64
Table 15. Obtained CWSI values with lysimeter and remote sensing calculations for west part of the research area.....	66

LIST OF FIGURES

Figure 1. CWSI depiction (Idso et al., 1982).....	9
Figure 2. Principles of remote sensing.....	12
Figure 3. Surface energy budget	15
Figure 4. General appearance of the research area located near Bushland, Texas is shown using ArcGIS 10.1	20
Figure 5. Location of weighing lysimeters (Evelt et al., 2012)	22
Figure 6. Comparison of Lysimeter measured ETa values with Remote Sensing obtained ETa values for North-east and South-east part of the research area.....	36
Figure 7. Comparison of Lysimeter measured ETa values with Remote Sensing obtained ETa values for North-west and South-west part of the research area	37
Figure 8. A comparison of Lysimeter-obtained rah values and remote sensing.....	39
Figure 9. A comparison of lysimeter-obtained To values and remote sensing-obtained To values	42
Figure 10. A comparison of lysimeter-obtained H values and remote sensing-obtained H values	45
Figure 11. A comparison of lysimeter-obtained Rn values and remote sensing-obtained Rn values	48
Figure 12. A comparison of lysimeter-obtained G values and remote sensing-obtained G values	50
Figure 13. A comparison of lysimeter-obtained ET values and remote sensing-obtained ET values for June 26 th	52
Figure 14. A comparison of lysimeter-obtained ET values and remote sensing-obtained ET values for July 12 th	53
Figure 15. A comparison of lysimeter-obtained ET values and remote sensing-obtained ET values for July 20 th	54
Figure 16. A comparison of lysimeter-obtained ET values and remote sensing-obtained ET values for July 28 th	56
Figure 17. A comparison of lysimeter-obtained ET values and remote sensing-obtained ET values for August 5 th	57
Figure 18. A comparison of lysimeter-obtained ET values and remote sensing-obtained ET values for August 13 th	58
Figure 19. A CWSI comparison for east part of the research area	63
Figure 20. A CWSI comparison for west part of the research area	65

CHAPTER 1:INTRODUCTION

Water is one of the most important limited natural resources on the globe, and the management of water resources is one of the greatest challenges for humankind in this century (Trezza, 2002). With the increasing population growth, pollution of natural resources, global warming, and climate change, water availability has become more significant for agriculture around the world (Colak et al., 2015). Furthermore, a major part of the world is struggling with water scarcity, so proper use of water is of great importance. The determination of the consumptive use of water by crops on the regional scale is elementary in understanding whether resource management is adequate (Bastiaanssen, 1998). Demand for food production, fiber, and fuel is increasing, and the economic yield of agricultural production per unit of water used is becoming a key criterion of success (Evelt et al., 2012).

1.1 Water Scarcity and Drought

Water is essential for life, but the pressure on water resources has become more significant with climate change, and population and economic growth. Water scarcity is defined as a situation in which insufficient water resources are available to satisfy long-term average requirements (Monzonis et al., 2015). Water scarcity is a widespread problem, especially for most of the semiarid regions around the world (Kahil et al., 2014). The impact of climate change on these regions is significant and will become more severe in the future. Water resource availability will decrease and frequent, longer, and more severe droughts will be experienced (Kahil et al., 2015). Increased water demand, insufficient water resources, and periodic occurrence of drought have brought tension to irrigated areas (Vila et al., 2007). To obtain a

maximum yield with limited water availability and drought conditions, it is necessary to develop effective irrigation management methods.

1.2 Population Growth

The world population is expected to rise above 9 billion by 2050, based on the United Nations' estimation. This population growth will increase the demand for fresh water supplies for agriculture purposes and consumer uses (Taft, 2015). Moreover, this increase in population will require about 60% more food (FAO, 2013), and therefore the proper management of irrigated agriculture is becoming more significant for the world's future food supply.

1.3 Global Warming and Climate Change

It is expected that climate change will bring increases in average global temperatures of between 1.4°C and 5.8°C by 2100 (DeNicola et al., 2015). These small changes in the average temperature will have a large impact on climate and weather. The only way to minimize the effect of global warming is to reduce the anthropogenic emissions of greenhouse gases.

However, with the increase of population and economic growth, dependence on energy is increasing daily. The significant reduction in carbon oscillation and the development of new low-carbon technologies are required to mitigate the effect of climate change (Ming et al., 2013). The most appropriate way to do this is by replacing old energy sources with new renewable energy sources.

Depending of the degree of climate change, many places have been seeing more intense rain, floods, and drought. These changes will significantly affect the quality and availability of water, as the hydrological cycle is strongly related to climate change, and specifically to greenhouse

gases in the Earth's atmosphere associated with global warming (DeNicola et al., 2015). It is necessary to be aware of the relationship between climate change and crop response to this change, as well as to develop new management strategies and adapt the farming system to climate change (He et al., 2014).

1.4 Irrigated Agriculture

Irrigation is the largest single consumer of water in the world: more than 80% of total fresh water is consumed for agricultural purposes (Hoffman et al., 2007). With the increase in population, attention to agriculture is increasing daily. Since agricultural areas are limited, it is necessary to use these limited areas efficiently to obtain a maximum yield.

About one third of the total world food production is obtained from agricultural production, which represents nearly 17% of the cropped area of the world. For the United States, about 12% of the cropped area is irrigated and creates 25% of all of the country's crops (Irmak, 2008). Thus, exact measurement of plant water use (evapotranspiration) is vital for efficient use of water resources and for planning and management purposes, especially for arid and semiarid regions.

Evapotranspiration (ET) is a process in which water is converted from liquid to vapor via evaporation from soil and wet plant surfaces and via transpiration of water from within plant tissue. Evaporation and transpiration occur simultaneously, and there is no easy way to distinguish between the two processes. In other words, land surface ET transfers large volumes of water (and energy, in the form of latent heat) from the soil (evaporation) and vegetation (transpiration) into the atmosphere (Anderson et al., 2011).

ET is a major component of the water budget and energy balance. It has long been recognized as the most important process in determining exchanges of energy and mass between the

atmosphere and biosphere (Sellers et al. 1996). Understanding the partitioning of ET will become increasingly important for sustainable management of water resources on regional scales (Zhao et al., 2015). About 57% of annual precipitation falling over the land is returned to the atmosphere by ET (Irmak, 2008).

On a field scale, ET can be measured over a homogenous surface by using conventional techniques and equipment such as the Bowen Ratio (BR), the Eddy Covariance (EC), and Lysimeter systems. However, these systems do not provide spatial distribution on a regional scale (Gowda et al. 2007). Remote sensing-based ET models are better suited to estimating crop water use on a regional scale (Allen et al. 2007a). Furthermore, remote sensing of surface energy balance for land provides instantaneous estimates of latent heat flux (LE) or ET (Chavez et al., 2010).

1.5 ASCE Standardized Reference ET Equation

Reference ET is modeled based on two types of surfaces, and it is improved or standardized by using appropriate constants for each type of surface. According to the American society of Civil Engineers and Environmental and Water Resources Institute (ASCE-EWRI (2005)), the ASCE-ET reference ET equation for the two surfaces is defined as follows.

Standardized Reference ET Equation for Short ET surfaces (ET_{0s}): Reference ET for a short crop with an approximate height of 0.12 m (similar to clipped, cool season grass).

Standardized Reference ET Equation for Tall ET surfaces (ET_{rs}): Reference ET for a tall crop with an approximate height of 0.50 m (similar to full-cover alfalfa).

Doorenbos et al. (1977) describe ET_o in FAO-24 as the rate of ET from an extensive surface of 8 to 15 cm tall green grass cover of uniform height that is actively growing, completely shading the ground, and not short of water.

The ASCE-EWRI (2005) standardized Penman-Monteith (PM) method has the following form:

$$ET_{sz} = \frac{0.408\Delta(R_n - G) + \gamma \frac{C_n}{T + 273} u_2 (e_s - e_a)}{\Delta + \gamma(1 + C_d u_2)} \quad (1.1)$$

Where ET_{sz} is the standardized reference crop ET for short and tall surfaces (mm d^{-1} for daily time steps or mm h^{-1} for hourly time steps); R_n is the calculated net radiation at the crop surface ($\text{MJ m}^{-2} \text{d}^{-1}$ for daily time steps or $\text{MJ m}^{-2} \text{hr}^{-1}$ for hourly time steps); G is soil heat flux density at the soil surface ($\text{MJ m}^{-2} \text{d}^{-1}$ for daily time steps or $\text{MJ m}^{-2} \text{hr}^{-1}$ for hourly time steps); T is mean daily or hourly temperature at 1.5 to 2.5 m height ($^{\circ}\text{C}$); u_2 is mean daily or hourly wind speed at 2 m height (m s^{-1}); e_s is saturation vapor pressure at 1.5 to 2.5 m height (kPa), calculated for daily time steps as the average of saturation vapor pressure at maximum and minimum temperature; e_a is mean actual vapor pressure at 1.5 to 2.5 m height (kPa); Δ is slope of the saturation vapor pressure-temperature curve ($\text{kPa } ^{\circ}\text{C}^{-1}$); γ is psychrometric constant ($\text{kPa } ^{\circ}\text{C}^{-1}$); C_n is the numerator constant that changes with reference type and calculation time step; and C_d is the denominator constant that changes with reference type and calculation time step.

C_n and C_d were obtained from simplifying many terms in the ASCE-EWRI (2005) standardized PM equation. C_n values take into account time step and aerodynamic roughness of the, and C_d values take into account time step, bulk surface resistance, and aerodynamic roughness of the surface. All calculation steps for calculating ETr are given in Appendix A

1.6 Crop Evapotranspiration

The ET rate from the crop surface is measured using the mass transfer or the energy balance method (Allen et al., 1998). Crop ET is calculated by multiplying reference ET by a crop coefficient, K_c as is presented in Eq. (1.2). Crop coefficients have been used to simplify and standardize the calculation of crop water use (Hoffman et al., 2007). Crop coefficient shows the ratio between the actual ET surface and the reference ET surface.

Crop coefficients can be expressed as a single coefficient factor, or they can be separated into two parts for soil and crop surfaces. In the single crop coefficient approach in Eq. (1.2), transpiration from crop and evaporation from soil are combined together and expressed as a single coefficient, K_c . This approach is used for irrigation system planning where averaged soil wettings are appropriate.

$$ET_c = K_c ET_o \quad (1.2)$$

Where ET_c is the crop ET (mm day^{-1}); ET_o is the reference crop ET (mm day^{-1}); and K_c is the crop coefficient (dimensionless).

In the dual crop coefficient approach, which needs more numerical calculations, transpiration from crop and evaporation from soil are evaluated separately, as it is shown in Eq. (1.3). The basal crop coefficient (K_{cb}) is used to express transpiration from the crop, while the soil water evaporation coefficient (K_e) is used to express evaporation from the soil. Crop ET is calculated by using Eq. (1.4).

$$K_c = K_{cb} + K_e \quad (1.3)$$

$$ET_c = (K_{cb} + K_e) \times ET_o \quad (1.4)$$

Where K_{cb} is the basal crop coefficient and K_e is the soil water evaporation coefficient.

Crop coefficients depend on the specific crop height, the albedo of the crop-soil surface, the canopy resistance, and the evaporation from the soil. As the crop grows, the crop height, crop leaf area index, and crop ground cover rate change all increase with the growing stage.

The main use of the crop coefficient is to help separate the actual crop surface from the reference crop surface. Wright (1982) states that crop coefficients improve irrigation time scheduling and estimation of crop water requirements with the improved estimation of ET.

1.7 Plant Water Stress

The relationship between the plant canopy and its thermal environment is a significant issue that specifies the plant growth and development process (Mahan et al., 2015). The plant canopy temperature is generally similar to the air surrounding it, but if the plant canopy is under a water deficit, the temperature of the plant canopy could be higher than the air surrounding it.

The water that a plant consumes depends on characteristics of the plant and on climate conditions. With the increasing of temperature, wind speed, and sunshine duration, the water consumption of plants increases since the ET rate is high in these conditions; conversely, with relative humidity increases, the water consumption of plant decreases since the ET rate is low in these conditions. Plant water consumption values are defined for short-term periods – daily, weekly, and 10-day periods or for long-term periods – monthly and seasonal periods. Short-term plant water consumption values are used to decide irrigation time and frequency, whereas long-term predictions are used to determine average plant water consumption for the irrigation area.

Water stress is caused by a lack of water supply in plant leaves, drought, or high soil salinity. The effect of water stress can change depending on plant species, and it has a major impact on plant growth and development. Under water stress conditions, the canopy temperature increases, since most of the energy absorbed is converted to sensible heat and is used to heat the plant surfaces instead of cooling the plant surfaces by evaporating water. Therefore, water stressed crops have higher temperatures than non-water stressed crops.

Plant leaf temperature is generally measured remotely by using an infrared thermometer (IRT). Infrared thermometry is the most preferable method for plant temperature studies since it does not require physical contact with the plant (Mahan et al., 2008), it can measure the temperature of one plant or of a whole area, it is nondestructive, and it is less expensive than alternative methods (DeJonge et al., 2015). The working principle of the IRT is that it senses the radiation that is emitted as long-wave radiation by plant canopies, converts it to an electrical signal, and displays it as a temperature.

Many methods have been developed for monitoring water stress. All of these methods are based on plant canopy temperature as a main source, which is measured one or two hours after solar noon, for quantifying water stress and determining an irrigation schedule. The stress degree day (SDD) procedure and crop water stress index (CWSI) are popular methods to evaluate water stress in plants (Kirkham, 2005). First, the SDD concept was developed by Jackson et al. (1977) and uses the difference between the plant canopy temperature (T_c) and the air temperature (T_a). If $T_c - T_a$ is negative, the plant leaves are well watered, while if the difference is positive, then the plants need irrigation. Gardner (1979) and Walker (1980) found that, used by itself, the difference between the plant leaf temperature and air temperature was not enough to estimate plant water stress status. Therefore, the method was improved with a new approach by Idso et al.

(1981a). This new approach estimated plant water status by considering air temperature, canopy temperature, and relative humidity. Subsequently, Idso et al. (1982) developed the CWSI concept, which is also known as the plant water stress index. This new approach of the plant water stress status considered the relationship between plant canopy temperature and air temperature difference ($T_c - T_a$) and vapor pressure deficit (VPD) in the standard conditions (Idso, 1982). The CWSI method is depicted in Figure 1.

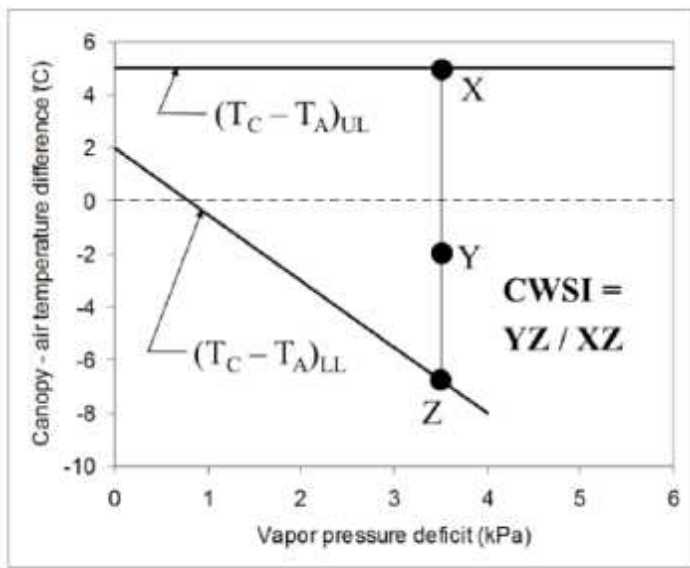


Figure 1. CWSI depiction (Idso et al., 1982)

The CWSI can also be calculated by using Eq. (1.6) from the ratio of actual and potential ET that was derived from the Penman-Monteith equation.

$$CWSI = 1 - \frac{E_a}{E_p} \quad (1.6)$$

Where E_a is actual ET and E_p is potential ET.

Jackson et al. (1981) conclude that the CWSI method is a promising method for measuring crop water stress. For better irrigation management practices, it is essential to know when plant water stress begins and how much water should be applied (Durigon et al., 2012).

1.8 Weighing Lysimeters

Lysimeters are containers or tanks of soils in which plants are grown (Howell et al., 1995). This is one of the methods that monitor the water balance for a small proportion of the surrounding area. Weighing lysimeters are a common method for measuring water loss from soil and plant surfaces and for developing crop coefficients for specific crops in estimating ET. The method measures ET as a difference in weight of the lysimeter (Abteu and Melesse, 2013). The conditions of the containers (such as plant density, height, leaf area of vegetation, and soil type) and surrounding area should be similar. Compared to traditional methods, weighing lysimeters is a highly accurate method for measuring ET from water balance. However, lysimeters are expensive equipment and require constant maintenance. Therefore, they are only preferred for research purposes.

1.9 Remote Sensing System

Photography was invented in 1826 (Lillesand et al., 2007). Remote sensing technology started with a balloon that carried a camera inside it. In 1858, a Parisian photographer obtained black and white images by using this system. Then, following the balloon experiment in 1858, a kite was flown equipped with a camera for meteorological purposes in 1882. In 1909, the first movie was made with a camera that was used in a plane. By the 1920s and 30s, government offices all over the world had started to use air photos to gather information about countries' natural and cultural resource bases.

Cameras have been used for over 150 years for remote sensing purposes. In the 1960s, the first meteorological satellite (TIROS -1) was launched and the first “remote sensing” term was subsequently used. Landsat-1 was that the first Earth resource satellite, and was launched in 1972. Since then, new Landsat satellites and other satellites (such as AVHRR, ASTER, and MODIS) have been produced for remote sensing purposes. The Landsat satellites have a high spatial resolution for the optical and mid infrared bands (30 m x 30 m), and their image size (scene or coverage) is 185 km x 172 km.

Remote sensing is the science and art of obtaining information about the Earth’s surface without being in contact with an object. This information can be obtained by detecting reflected and emitted energy, recording and analyzing that energy, and then applying that information (Lillesand et al., 2007).

Remote sensing systems can be classified as active and passive remote sensing based on their detection basics, camera, and scanner systems, as well as on their function. The sun is the main source of electromagnetic energy or radiation. This electromagnetic energy must be reflected, absorbed, or emitted. Passive sensors rely on energy from the sun, whereas active sensors have their own energy source and do not depend on the sun. Active sensors send energy directly to the target from their own energy source, and then receive reflected energy from the target.

The working principles of remote sensing systems are presented in Figure 2. The first requirement of a remote sensing system is a source of energy, such as the sun or electromagnetic energy from another source. As energy travels towards its target through the atmosphere, it interacts with the atmosphere. This interaction happens a second time when the energy travels from the target through the sensor. When the energy reaches the Earth’s surface, it interacts with

the target and, depending on the target and radiation features, this energy is scattered or emitted from the target. Electromagnetic energy is collected and recorded. The recorded energy is then sent to the process station, generally in electronic form, and the station later processes the image. Subsequently, the image of the target is evaluated visually, digitally, or electronically. Finally, the information obtained from the remote sensing process is used in the area where it is needed.

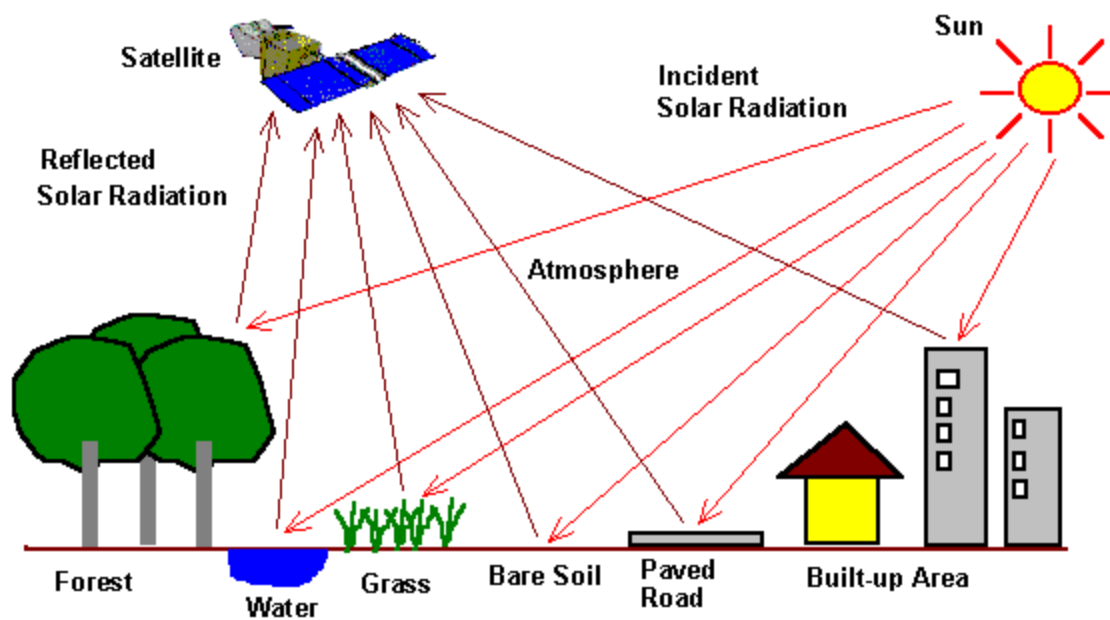


Figure 2. Principles of remote sensing

Electromagnetic energy can be described by either wavelength or frequency. Wavelength and frequency are related and have an inverse relationship. The longer the wavelength (λ) is, the lower the frequency (ν), and vice versa.

Remote sensing systems create images by recording target responses (reflectance, temperature) on different bands along the electromagnetic spectrum. The electromagnetic spectrum ranges between shorter wavelengths, which are gamma- and x-rays, and longer wavelengths, which include microwaves, and TV and radio waves. The ultraviolet (UV) portion of the spectrum,

which is ranked between 0.2 and 0.4 μm , is used for most remote sensing applications. The visible portion of the spectrum can be detected by the human eyes. The wavelength in this visible portion ranges between 0.4 and 0.7 μm . There are six colors in the visible portion of the spectrum: violet ranges from 0.4 to 0.446 μm , blue from 0.446 to 0.500 μm , green from 0.500 to 0.578 μm , yellow from 0.578 to 0.592 μm , orange from 0.592 to 0.620 μm , and the longest visible wavelength is red and ranges from 0.620 to 0.7 μm . Blue, red, and green are the primary colors and all other colors are created by using these primary colors.

The infrared (IR) portion of the spectrum is ranked between 0.7 and 100 μm . The infrared portion is divided into two parts: reflected IR, which is ranked between 0.7 μm and 3 μm ; and thermal IR, which is ranked between 3.0 and 100 μm . While the reflected IR portion resembles the visible portion of the spectrum, the thermal IR portion has a different purpose than the visible and reflected IR portion since the energy that is emitted in the thermal portion is in the form of heat.

The microwave portion of the spectrum is ranked between 1 mm and 1m; these are the longest wavelengths, and are also used for remote sensing applications. The shorter wavelengths have properties similar to the thermal infrared region, while the longer wavelengths are used for radio broadcast.

All electromagnetic energy that reaches the Earth's surface must be scattered, absorbed, and transmitted. Boltzmann conducted research on the radiometric temperature of objects and reports that the total energy radiated from a surface is proportional to the fourth power of its absolute temperature. The Stefan Boltzmann law indicates that with the increase of temperature, the amount of radiation that is emitted also increases.

1.9.1 Remote Sensing Models for Estimating ET

Remote sensing applications have been used in a wide range of areas, such as for land use and land cover mapping, geological and soil mapping, water resource management purposes (pollution detection, lake eutrophication assessment, flood damage estimates), agricultural purposes, wetlands and landform mapping, environmental assessment, wild life ecology, and archaeological applications. Mapping ET is one of those areas that commonly use remote sensing applications.

Most of the remote sensing models are based on the energy balance equation to estimate ET. As it is shown in Figure 3 and Eq. (1.10), the energy balance equation model R_n , G, and H, and determines LE as a residual.

$$R_n - LE - G - H = 0 \quad (1.10)$$

Where LE is the latent heat flux (W m^{-2}); R_n is the net radiation (W m^{-2}); G is the soil heat flux (W m^{-2}); and H is the sensible heat flux (W m^{-2}). R_n is positive towards the crop surface, whereas LE and H are positive away from the crop surface, and G is positive into the soil. The energy balance equation to estimate the ET can be applied to large and homogenous surfaces.

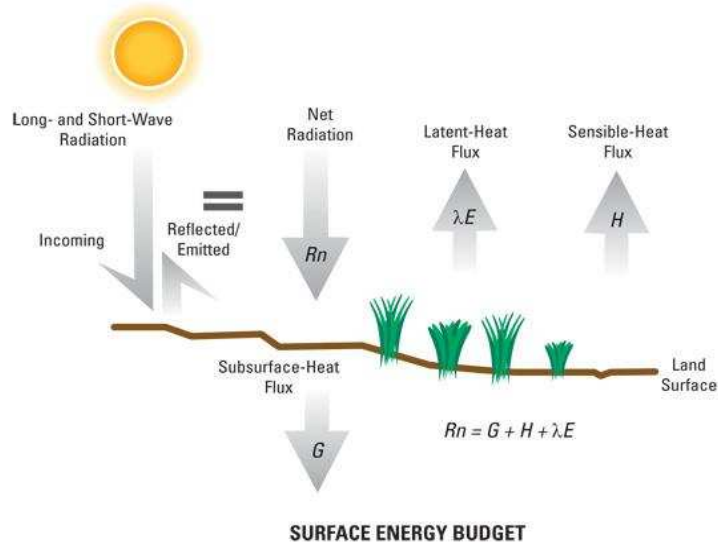


Figure 3. Surface energy budget

Remote sensing-based energy balance equations estimate the latent heat flux (LE) as an instantaneous LE value. Below, Equations (1.11) and (1.12) are used to convert an instantaneous LE to an ET value. ET is estimated in the units of mm d^{-1} or mm h^{-1} .

$$\lambda = 2.501 - 0.00236T_a \quad (1.11)$$

$$ET = \frac{t \times LE}{\lambda \times \rho_w} \quad (1.12)$$

Where λ is the latent heat of vaporization (MJ kg^{-1}); T_a is the air temperature ($^{\circ}\text{C}$); t is the time constant (3,600 seconds for the computation of one hour); and ρ_w is the density of water ($1,000 \text{ kg m}^{-3}$).

The advantage of a remote sensing system compared to other systems such as the Bowen Ratio, the Eddy Covariance, and Lysimeters to estimate ET is that remote sensing systems cover much larger areas than the other methods. In addition, it is relatively cheap and fast for the investigation of large area. The system enables the collection of up-to-date and permanent

information about the area and provides information in several wavelengths, even if it is not visible with the naked eye. Furthermore, it also enables researchers to know the conditions of an area without visiting it. In addition, the ET rate can be measured in several areas by using remote sensing-based ET modeling, which is highly important for water management studies (Bastiaanssen et al., 2001).

1.10 The Surface Aerodynamic Temperature (SAT) Model

The EB algorithm requires the computation of net radiation (R_n), soil heat flux (G), and sensible heat flux (H) to solve for ET as a residual. By using this algorithm, R_n and G can be estimated with an acceptable accuracy. However, for computing H , instead of surface aerodynamic temperature (T_o), radiometric surface temperature (T_s) is generally used. Using T_s may cause overestimation of H , since T_s is larger than T_o in most instances. According to Choudhury et al. (1986), radiometric surface temperatures are higher than aerodynamic surface temperatures for stable atmospheric conditions, and lower than aerodynamic temperatures for unstable atmospheric conditions; these two temperatures were about the same for near-neutral atmospheric conditions. Chehbouni et al. (1996) state that the difference between the aerodynamic and radiometric surface temperatures is small for the dense canopy conditions, but that, regarding the sparse vegetation conditions, the difference between the two temperatures can exceed 10°C . Thus, temperature differences cause over estimation of sensible heat flux, which is a significant part of the surface energy budget.

Brutsaert (1982) suggest that formulating the relationship between aerodynamic and radiometric surface temperature is useful for the accurate quantification of ET. According to Hall et al. (1992), however, finding a relationship between these two temperatures is highly difficult since

radiometric surface temperature is a function of radiometric and kinetic temperature of the surface, sensor view angle, and surface morphology, whereas aerodynamic surface temperature is a function of the radiometric and kinetic temperature and the thermodynamic properties of air in contact with a surface.

Boulet et al. (2012) define the aerodynamic surface temperature as an average temperature of the air in the vicinity of the vegetation elements within the canopy, at the height of the aerodynamic level (sum of the displacement height and the roughness length for momentum); therefore, there is no measuring device for this temperature. For homogeneous surfaces, T_o and T_s values are nearly equivalent, but for heterogeneous surfaces there are important differences between the two. Therefore, for heterogeneous surface conditions there may be instances of underestimation of ET. To account for those differences between T_o and T_s , several remote sensing-based algorithms have been developed for mapping ET. The Surface Aerodynamic Temperature (SAT) model is one of the models that have been developed to establish a relationship between these two temperatures.

The SAT model was used in the present study. It estimated surface aerodynamic temperature (T_o) based on surface radiometric temperature (T_s), air temperature (T_a), and bulk surface aerodynamic resistance (r_{ah}) for cotton fields in the Texas Panhandle. In this study, sensible heat flux (H) values were computed by using the T_o model, and ET values were calculated as a residual of energy balance for research fields located at the USDA-ARS CPRL near Bushland, Texas for the year of 2008.

1.11 Objectives

The objectives of this study are the following:

- 1) To use the SAT model to estimate sensible heat flux (H) for cotton fields, and to calculate ET as a residual of the EB for research fields located at the USDA-ARS CPRL near Bushland, Texas for 2008.
- 2) To compare ET results obtained from the multispectral airborne remote sensing data and the SAT model with actual ET measured and calculated by mass balance by using large weighing lysimeters, which were located in the center of each field, and computing statistics to determine the accuracy of the SAT ET remote sensing method.
- 3) To calculate crop water stress from the actual ET that was obtained from remote sensing by using ArcGIS and potential ET that was obtained from a Reference Evapotranspiration (REF-ET) calculator. And to evaluate the method using lysimetric data.

CHAPTER 2: METHODOLOGY

2.1 Site Description

The Bushland ET and Agricultural Remote Sensing Experiment was conducted at the USDA-ARS CPRL near Bushland, Texas in 2008. The geographic coordinates of the area are 35° 11` N, 102° 06` W, and the elevation is 1,170 m above mean sea level. The area is primarily surrounded by the 486.000 ha Pullman soils, fine, mixed, and super active. Slopes vary between 0 to 0.5% in most parts of the study area. The major crops in the region are corn, sorghum, winter wheat, and cotton. The overview of the study area in ArcGIS 10.1 is given in Figure 4. The main reason for choosing the Bushland area for this study was the high ET demand in the area (Evetts et al., 2012).



Figure 4. General appearance of the research area located near Bushland, Texas is shown using ArcGIS 10.1

2.2 Weighing Lysimeter Data

The lysimeters and surrounding areas were planted with cotton. The research area comprised four fields: the south-east, south-west, north-east, and north-west lysimeter fields. The west fields were under a dryland regime, while the east fields were fully irrigated with a lateral move sprinkler system. Ground-based crop water use or ET was derived from large weighing lysimeters (3 m long x 3 m wide x 2.4 m deep) that were situated in the middle of each field (Figure 5). Near the lysimeter there was one net radiometer (Q*7.1, Radiation and Energy Balance Systems [REBS], Bellevue, Wash.) and two infrared thermometers (model IRT/c2, Exergen) for measuring R_n and T_s , respectively. In addition, the following sensors completed the instrumentation at the lysimeter location: four soil heat flux plates (HFT3, REBS, Campbell Scientific, Inc. [CSI], Logan, Utah), four averaging soil temperature thermocouple probes (TCAV-L, CSI, Logan, Utah), an albedo meter (CM-14, Kipp & Zonen, Bohemia, N.Y.), and a tipping-bucket rain gauge (model 6011B, Qualimetrics, Inc., Sacramento, Cal.) (Chávez et al., 2010).

Canopy height, Leaf Area Index (LAI), and surface albedo values were used for lysimeter calculations in Excel for applying the SAT model for the actual ET calculations, and were taken from remote sensing-based calculations in ArcGIS 10.1. When applying the SAT model, a multiple linear regression approach was used for the calculation of aerodynamic surface temperature (T_o) and surface aerodynamic resistance (r_{ah}) in Excel for lysimeter calculations of ET_a . Then, sensible heat flux (H) values were computed as a function of T_o , T_a , and r_{ah} . ET_a was calculated as a residual of the energy balance equation. All calculation steps were performed in Excel for lysimeter ET_a calculations and can be found in Appendix B in detail. Beside the

Lysimeter ETa calculations in Excel, lysimeter measured ETa values were compared with remote sensing obtained ETa values by using SAT model.

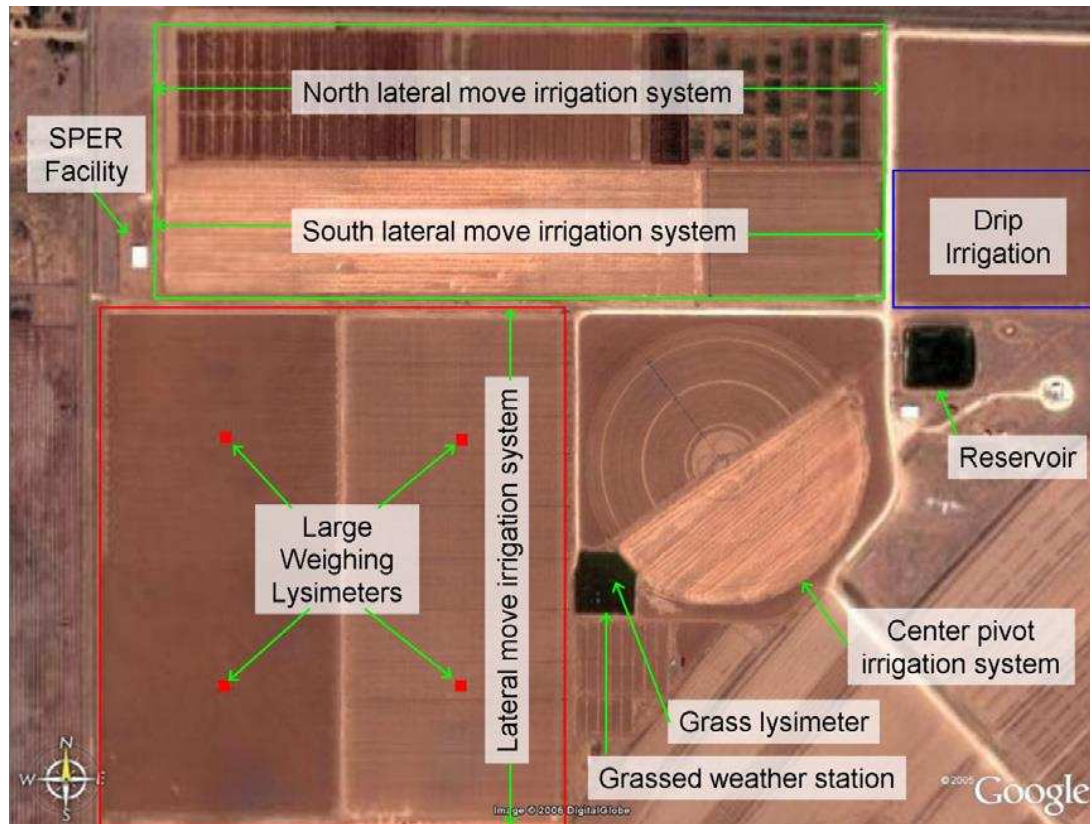


Figure 5. Location of weighing lysimeters (Evelt et al., 2012)

2.3 Meteorological Data

Based on airborne remote sensing data, six days of the year were used to map ET in this study: June 26th, July 12th, July 20th, July 28th, August 5th and August 13th of 2008. Weather data for the months were obtained from the Texas High Plains ET Network (TXHPET, 2008). In addition to the main weather station, meteorological data were collected from small weather stations that were placed near lysimeters locations. Monthly average air temperature values were 2°C lower than long term averages. However, for the month of July, temperature values were 0.8°C higher

than normal values. To grow cotton in this area, an average of 670 mm of water is required.

During the 2008 cotton growing season in the research area, there was just 325 mm of rainfall (Chávez et al., 2010).

Table 1 below presents the weather variables (air temperature, wind speed, relative humidity, shortwave radiation, and barometric pressure) measured on a grass field near the research area on the days of remote sensing system overpasses.

Table 1. Weather data used for remote sensing calculation

WEATHER VARIABLES							
DATE	DOY	CST	Rs (W/m ²)	Tair (°C)	RH (%)	BP (Pa)	u (m/s)
26-Jun-08	178	10:52	826.2	29.8	34	88400	7.8
12-Jul-08	194	11:20	897.3	21.6	44	88900	9.0
20-Jul-08	202	11:06	805.4	27.5	44	89000	4.5
28-Jul-08	210	11:24	844.3	29.5	50	88100	5.3
5-Aug-08	218	11:43	834.4	31.9	28	88900	2.4
13-Aug-08	226	11:25	825.7	25.9	53	88600	4.7

Tables 2-5 present the measured weather variables with the equipment's that were positioned on large weighing lysimeters for the North-east, North-west, South-east, and South-west parts of the research area.

Table 2. North-east lysimeter weather data

NORTH-EAST LYSIMETER WEATHER DATA					
DATE	CST	RH (%)	Tair (°C)	u (m/s)	NE_IRT (°C)
26-Jun-08	11:00	33.86	30.77	7.53	38.44
12-Jul-08	11:20	44.68	21.64	7.86	28.00
20-Jul-08	11:00	44.00	27.86	4.11	31.62
28-Jul-08	11:30	47.38	30.59	5.27	29.49
5-Aug-08	11:45	33.36	32.03	1.89	29.79
13-Aug-08	11:30	51.94	26.87	3.88	25.74

Table 3. North-west lysimeter weather data

NORTH-WEST LYSIMETER WEATHER DATA					
DATE	CST	RH (%)	Tair (°C)	u (m/s)	NW_IRT (°C)
26-Jun-08	11:00	33.48	31.00	7.38	38.03
12-Jul-08	11:20	43.00	21.77	8.29	33.42
20-Jul-08	11:00	38.47	28.89	4.47	38.61
28-Jul-08	11:30	42.00	31.75	5.64	35.84
5-Aug-08	11:45	33.39	34.03	2.19	47.79
13-Aug-08	11:30	46.29	27.92	4.85	28.87

Table 4. South-east lysimeter weather data

SOUTH-EAST LYSIMETER WEATHER DATA					
DATE	CST	RH (%)	Tair (°C)	u (m/s)	SE-IRT (°C)
26-Jun-08	11:00	33.55	31.07	7.25	37.65
12-Jul-08	11:20	45.39	21.66	7.54	28.36
20-Jul-08	11:00	41.78	28.32	4.54	26.37
28-Jul-08	11:30	45.26	31.20	5.47	27.01
5-Aug-08	11:45	29.94	32.55	2.02	26.68
13-Aug-08	11:30	50.80	27.29	4.13	24.06

Table 5. South-west lysimeter weather data

SOUTH-WEST LYSIMETER WEATHER DATA					
DATE	CST	RH (%)	Tair (°C)	u (m/s)	SW-IRT (°C)
26-Jun-08	11:00	33.48	31.00	7.38	38.78
12-Jul-08	11:20	43.00	21.77	8.29	32.74
20-Jul-08	11:00	38.47	28.89	4.47	36.70
28-Jul-08	11:30	42.00	31.75	5.64	35.43
5-Aug-08	11:45	33.39	34.03	2.19	45.74
13-Aug-08	11:30	46.29	27.92	4.85	27.22

2.4 Remote Sensing Data

The remote sensing data, acquired with the Utah State University (USU) multispectral airborne system, comprised high-resolution multispectral images in the visible, near-infrared (NIR), and thermal infrared (TIR) portions of the electromagnetic spectrum. The three band images consisted of three layers: NIR (0.790-0.810 μm), red (0.665-0.675 μm), and green (0.545-0.555 μm). To map ET, NIR, red, and thermal bands were used. NIR and RED bands were used for the derivation of vegetation indices such as the Optimized Soil Adjusted Vegetation Index (OSAVI), LAI, the canopy height and surface albedo, and implicitly soil heat flux, while the thermal infrared band was used for obtaining the surface temperature. In addition, the thermal band was used to derive the SAT model and to estimate the net radiation. The surface temperature derived from the thermal band was also used to estimate the sensible heat flux.

ArcGIS 10.1 was used to map ET for the Bushland, Texas research area. First, the research area was separated into four parts (SE, NE, SW, and NW) by using editor and clipping data management tools. All calculations were done in Model Builder in ArcGIS 10.1 using the raster calculator tool. The same procedure was followed for the lysimeter calculations of ET_a in Excel with some common inputs for remote sensing calculations. Each calculation step that is presented in Section 2.4 is detailed in Appendix C, Modeling SAT, along with the modeling steps.

The SAT model was used in this study to estimate T_o based on T_s , air temperature (T_a), and surface aerodynamic resistance (r_{ah}) for cotton fields. Sensible heat flux was computed by using the T_o model and ET was calculated as a residual of EB for research fields located at the USDA-ARS CPRL near Bushland, Texas for the year of 2008.

The results obtained from the multispectral airborne remote sensing data and the ET algorithms were compared to lysimeter-based ET from the middle of each research area.

The SAT Model that was used in this study was improved by Chávez et al. (2010).

$$T_o = 0.5 T_s + 0.5 T_a + 0.15 r_{ah} - 1.4 \quad (2.1)$$

Where T_o is the surface aerodynamic temperature ($^{\circ}\text{C}$); T_s is the surface radiometric temperature ($^{\circ}\text{C}$); T_a is the air temperature at screen height ($^{\circ}\text{C}$); and r_{ah} is the surface aerodynamic resistance (s m^{-1}).

The calculations steps are given below.

Surface albedo values were calculated with Eq. (2.2) using ArcGIS 10.1, and then the obtained surface albedo values were used for lysimeter calculations of R_n in Excel.

$$\alpha = 0.512 NIR + 0.418 RED \quad (2.2)$$

Where α is the surface albedo; NIR is the reflectance in the near-infrared portion of the spectrum; and RED is the reflectance in the red portion of the spectrum.

OSAVI was calculated with NIR and RED bands with Eq. (2.3):

$$OSAVI = \frac{(1.16) \times (NIR - R)}{(NIR + R + 0.16)} \quad (2.3)$$

Where OSAVI is the Optimized Soil Adjusted Vegetation Index (Rondeaux et al., 1996); NIR is the reflectance in the near-infrared portion of the spectrum; and RED is the reflectance in the red portion of the spectrum.

Then LAI was calculated with OSAVI obtained from Eq. (2.3), Chávez et al., (2009b):

$$LAI = 0.263e^{(3.83 \text{ OSAVI})} \quad (2.4)$$

Where LAI is the Leaf Area Index ($\text{m}^2 \text{m}^{-2}$)

Two equations were used for the east (Eq. (2.5)) and west (Eq. (2.6)) fields (Chávez J.L., personal communication) of the research area:

$$hc_{east} = 0.163784LAI + 0.195938 \quad (2.5)$$

$$hc_{west} = 0.052221LAI + 0.457288 \quad (2.6)$$

Where hc_{east} is the height of the vegetation on the east side of the research area (m), and hc_{west} is the height of the vegetation on the west side of the research area (m). Obtained crop height values from remote sensing calculations were used for lysimeter calculations of roughness length parameters in Excel for the calculation of other inputs.

After calculating crop height, it was used to calculate roughness lengths (Eq. (2.7) and (2.8)) and zero plane displacement (Eq.(2.9)):

$$z_{om} = 0.123 \times h_c \quad (2.7)$$

$$z_{oh} = 0.1 \times z_{om} \quad (2.8)$$

$$d = 0.67 \times h_c \quad (2.9)$$

Where h_c is the crop height (m); z_{om} is the roughness length for the momentum transfer (m); z_{oh} is the roughness length for the heat transfer (m); and d is the zero plane displacement height (m).

Surface aerodynamic resistance values were calculated for both the lysimeter and remote sensing methods by using Eq. (2.10):

$$r_{ah} = \frac{\ln\left(\frac{z-d}{z_{om}}\right) \ln\left(\frac{z-d}{z_{oh}}\right)}{uk^2} \quad (2.10)$$

Where r_{ah} is the surface aerodynamic resistance for neutral atmospheric conditions ($s\ m^{-1}$); z is the height from the ground at which the wind speed and air temperature were measured (m); z_{om} is the roughness length for the momentum transfer (m); z_{oh} is the roughness length for the heat transfer (m); d is the zero plane displacement (m); u is the horizontal wind speed ($m\ s^{-1}$); and k is the von Karman constant (0.41).

The iteration process was applied to calculate the sensible heat flux by using Eq. (2.11):

$$H = \frac{\rho_a C_{pa} (T_o - T_a)}{r_{ah}} \quad (2.11)$$

Where H is the sensible heat flux ($W\ m^{-2}$); ρ_a is the air density ($kg\ m^{-3}$); C_{pa} is the specific heat of dry air ($1005\ J\ kg^{-1}\ K^{-1}$); T_o is the aerodynamic surface temperature ($^{\circ}C$); T_a is the near-surface air temperature ($^{\circ}C$); and r_{ah} is the surface aerodynamic resistance ($s\ m^{-1}$) (Brutsaert's (1975,1982)).

Based on the results of Eq. (2.12), stable ($L_{M_o} > 0$) and unstable ($L_{M_o} < 0$) atmospheric conditions, two different ways were followed.

$$L_{M_o} = \frac{-u *^3 T_a \rho_a C_{pa}}{gkH} \quad (2.12)$$

Where L_{M_O} is the Monin-Obukhov stability lengths scale (m); u_* is the friction velocity (m s^{-1}); T_a is the surface air temperature (K); ρ_a is the air density (kg m^{-3}); C_{pa} is the specific heat of dry air ($1005 \text{ J kg}^{-1} \text{ K}^{-1}$); g is the gravity acceleration (9.81 m s^{-2}); and k is the von Karman constant (0.41).

The stability correction factor for atmospheric heat transfer and momentum transfer for unstable atmospheric conditions ($L_{M_O} < 0$) can be determined using the Businger-Dyer formulations (Eq. (2.13)) (Dyer and Hicks, 1970; Dyer, 1974; Businger, 1988; Sugita and Brutsaert, 1990):

$$\psi_h \left(\frac{z-d}{L} \right) = 2 \ln \left(\frac{1+x^2}{2} \right) \quad (2.13)$$

Where ψ_h is the stability correction factor for the atmospheric heat transfer; z is the height from the ground at which the wind speed and air temperature were measured (m); d is the zero plane displacement height (m); and L is the Monin-Obukhov stability length scale (m).

The stability correction factor was calculated using Eq. (2.14):

$$\psi_m \left(\frac{z-d}{L} \right) = 2 \ln \left(\frac{1+x}{2} \right) + \ln \left(\frac{1+x^2}{2} \right) - 2 \operatorname{atan}(x) + \frac{\pi}{2} \quad (2.14)$$

Where ψ_m is the stability correction factor for the momentum transfer; z is the height from the ground at which the wind speed and air temperature were measured (m); d is the zero plane displacement (m); and L is the Monin-Obukhov stability length scale (m).

$$x = 1 - \left(16 \left(\frac{z-d}{L_{M_O}} \right) \right)^{0.25} \quad (2.15)$$

For stable atmospheric conditions ($L_{M_0} > 0$), Webb (1970) suggests the following:

$$\psi_m \left(\frac{z-d}{L} \right) = \psi_h \left(\frac{z-d}{L} \right) = -5 \left(\frac{z-d}{L} \right) \quad (2.16)$$

Where ψ_m the stability correction factor for the momentum is transfer, and ψ_h is the stability correction factor for the atmospheric heat transfer.

Friction velocity was corrected for atmospheric conditions by using the Monin-Obukhov similarity theory in Eq. (2.17):

$$u_* = \frac{uk}{\ln \left(\frac{z-d}{z_{om}} \right) - \psi_m \left(\frac{z-d}{L} \right) + \psi_m \left(\frac{z_{om}}{L} \right)} \quad (2.17)$$

Then, surface aerodynamic resistance was calculated as in Eq. (2.18):

$$r_{ah} = \frac{\ln \left(\frac{z-d}{z_{oh}} \right) - \psi_h \left(\frac{z-d}{L} \right) + \psi_h \left(\frac{z_{oh}}{L} \right)}{u_* k} \quad (2.18)$$

The final equation (2.18) was used for the calculation of the surface aerodynamic temperature that was improved by Chávez et al. (2010).

Then, net radiation (Rn) was calculated with the incoming short wave radiation that was measured in the weather station located near the research area, along with air temperature and surface temperature, as shown in Eq. (2.19):

$$R_n = (1 - \alpha)R_s + (\epsilon_a \sigma T_a^4) - (\epsilon_s \sigma T_s^4) \quad (2.19)$$

Where R_n is net radiation (W m^{-2}); α is the surface albedo; R_s is the incoming shortwave radiation (W m^{-2}); ε_a is the emissivity of air; ε_s is the surface emissivity; σ is the Stefan Boltzmann constant ($5.67 \text{ E-}8 \text{ W m}^{-2} \text{ K}^{-4}$); T_a is the air temperature (K); and T_s is the surface temperature (K).

Soil heat flux was calculated with the net radiation and LAI that were estimated with remote sensing calculations using Eq. (2.20):

$$G = R_n(0.3324 - 0.024LAI)(0.8155 - 0.3032 \text{ LN}(LAI)) \quad (2.20)$$

Where G is the soil heat flux (W m^{-2}); R_n is the net radiation (W m^{-2}); and LAI is the Leaf Area Index ($\text{m}^2 \text{ m}^{-2}$).

Finally, latent heat flux was calculated as a residual of net radiation, soil heat flux, and sensible heat flux, as is expressed in Eq. (2.21):

$$LE = R_n - G - H \quad (2.21)$$

Where LE is the latent heat flux (W m^{-2}); R_n is the net radiation (W m^{-2}); G is the soil heat flux (W m^{-2}); and H is the sensible heat flux (W m^{-2}).

For converting instantaneous LE to daily ET value, Eq. (2.22) and Eq. (2.23) were. ET was estimated in the units of mm d^{-1} or mm h^{-1} .

$$\lambda = 2.501 - 0.00236 T_a \quad (2.22)$$

$$ET = \frac{t \times LE}{\lambda \times \rho_w} \quad (2.23)$$

Where λ is the latent heat of vaporization (MJ kg^{-1}); T_a is the air temperature ($^{\circ}\text{C}$); t is the time constant (3,600 seconds for the computation of one hour); and ρ_w is the density of water ($1,000 \text{ kg m}^{-3}$).

2.5 Calculation of Water Stress

The ET results obtained from the remote sensing data and the reference ET results obtained using the Reference evapotranspiration (REF-ET) calculator were used to calculate the water stress factor. Eq. (2.24) was used for the calculation of CWSI.

$$CWSI = 1 - \frac{ET_a}{ET_p} \quad (2.24)$$

$$ET_c = K_c ET_o \quad (2.25)$$

Where ET_c is the crop ET (mm day^{-1}), ET_p is the potential ET (mm day^{-1}), for standard conditions (no stress) ET_c is equal to ET_p ; ET_o is the reference crop ET (mm day^{-1}); and K_c is the crop coefficient (dimensionless).

Calculation steps are given in detail in Appendix D.

2.6 Statistical Analysis

Observing the accuracy of the SAT model and CWSI method, the actual ET results obtained from the multispectral airborne remote sensing data were compared with ET measured by mass balance by using large weighing lysimeters located in the center of each field. Mean biased error (MBE) and root mean squared error (RMSE) were calculated.

The MBE is the difference between mean of the model predicted variable (P) and the observed variable (O).

$$MBE = N^{-1} \sum_{i=1}^N (P_i - O_i) \quad (2.25)$$

The average difference can be described by the RMSE:

$$RMSE = \left[N^{-1} \sum_{i=1}^N (P_i - O_i)^2 \right]^{0.5} \quad (2.26)$$

CHAPTER 3: RESULTS AND ANALYSIS

3.1 Comparison of Lysimeter Measured ETa Values with Remote Sensing Estimated ETa Values

SAT model Remote Sensing obtained cotton ETa values were compared to Lysimeter measured ETa values. As it was mentioned before, the east fields of the research area were fully irrigated and the west fields were under a dryland regime. Thus, measured and estimated ETa values were higher for the east fields of the research area for both lysimeters and remote sensing SAT system.

Lysimeter measured ETa values were lower than remote sensing estimated ETa values (Figure 6) for all dates except in the beginning of the cotton growing season (June 26th and July 12th) for the east part of the research area. Even though measured Ta, RH, and u values were very close for both methods for this date, there was a large difference between the ETa values on these two days. The difference was mostly because of the SAT model that was used for remote sensing calculations of ETa. The SAT model applied by using airborne multispectral imagery and weather station data resulted in larger ETa (mm/h and mm/d) errors especially in the beginning of the growing season for both the east and west part of the research area. Comparison of ETa values resulted in a 25.90% MBE and 44.07% RMSE for the east part of the research area.

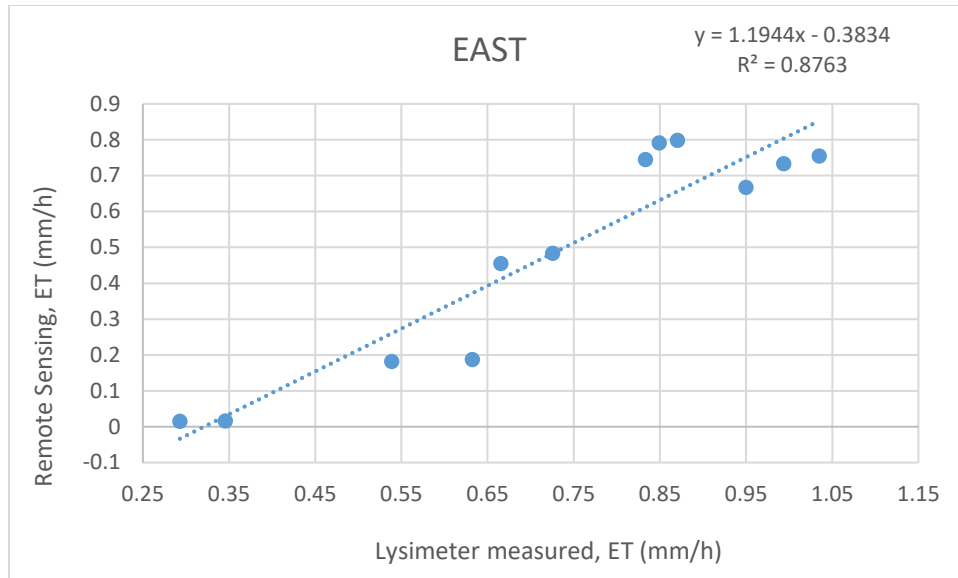


Figure 6. Comparison of Lysimeter measured ETa values with Remote Sensing obtained ETa values for North-east and South-east part of the research area.

In the beginning of the growing season, obtained h_c and LAI values were very small, which resulted in large errors in SAT model estimated ETa for both east and west research area. For the first two research dates (June 26th and July 12th), estimated ETa values were negative (Figure 7), except the NW part of the research area on June 26th. This result shows the low applicability of the model when LAI and h_c values were very small. For NW and SW fields of the research area managed under a dryland regime, the corresponding error that was observed was MBE of 42.13% and RMSE of 42.91%. This is a large over prediction of hourly ETa with remote sensing calculations. Large errors could be the results of sparse vegetation conditions and low vegetation density ($LAI < 0.5 \text{ m}^2/\text{m}^2$) in the beginning of the growing season. Estimating LAI with accuracy is very important since it is used for accounting for the temperature differences between soil and vegetation and the calculation of G.

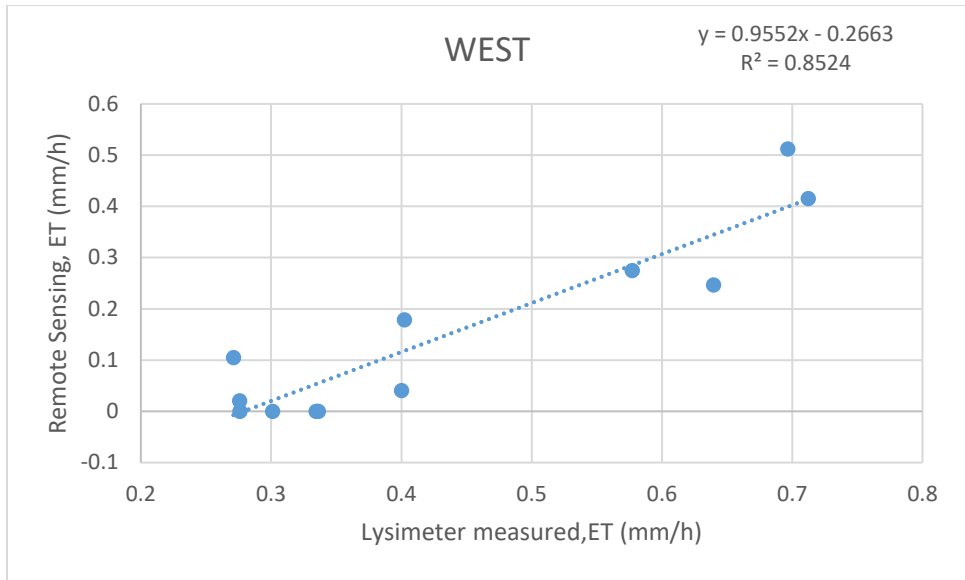


Figure 7. Comparison of Lysimeter measured ETa values with Remote Sensing obtained ETa values for North-west and South-west part of the research area

For the west field of the research areas, the sparse vegetation conditions might have caused some errors in the estimation of rah. Brutseart (1982) stated that there is a linear relationship between zom, zoh and hc for homogeneous surface conditions but for heterogeneous surface conditions there might be error into the computation of u* and rah which cause errors estimation of H and LE. If the sparse vegetation conditions considered as a heterogeneity, hc is critical for the estimation of H. The difference was examined between hc and LAI values for both remote sensing calculations and actual measurements at the lysimeters location. Remote sensing obtained hc and LAI values were higher than at lysimeter measured values which caused overestimation of actual ET with remote sensing calculations. Since the LAI values were used for the estimation of G in remote sensing calculations, G values overestimated with remote sensing calculations as well. In regard of Rn, remote sensing estimated Rn values were close to values measured at the lysimeter site.

On the other hand, instead of T_o , T_s was used for the estimation of H in the lysimeter based ETa calculations in MS Excel. T_s values were higher than calculated T_o values for all six dates. The higher T_s values resulted with overestimation of H, thus underestimation of ETa. Especially in the beginning of the growing season all ETa values were estimated as negative values.

Additionally, another aerodynamic surface temperature model developed by (Chávez et al., 2010) was applied to the lysimeter based ETa calculations in MS Excel. This other model is a function of T_s , T_a , LAI and u ($T_o = 0.57 T_s + 0.14 T_a + 0.81 LAI - 0.97 u + 14.9$). The performance of SAT model for estimating T_o was compared with the other aerodynamic surface temperature model. The obtained results show that in the beginning of the growing season, the new T_o model performed better than the previous SAT model tested for estimating ETa since this new T_o model is accounting for LAI when calculating T_o .

3.2 Comparison of at Lysimeter Calculated ETa Values with Remote Sensing Estimated ETa Values by Using SAT Model

3.2.1 rah Estimation

Two different equations were used for the computation of canopy heights in remote sensing calculations for the east and west sides of the research area which were function of LAI.

Subsequently, the average canopy heights were obtained for each area (south-east, south-west, north-east, and north-west) and for each date (June 26th, July 12th, July 20th, July 28th, August 5th, and August 13th) by using NIR and red bands from remote sensing calculations. Estimated average canopy heights from remote sensing calculations were used in Excel with lysimeter calculations for the computation of rah. Figure 8 shows the comparison of lysimeter-obtained rah values with remote sensing-obtained rah values. As is shown in Figure 6, lysimeter- measured

rah values were close to the remote sensing-estimated rah values for most of the dates, with an MBE of 5.21% and an RMSE of 15.69%.

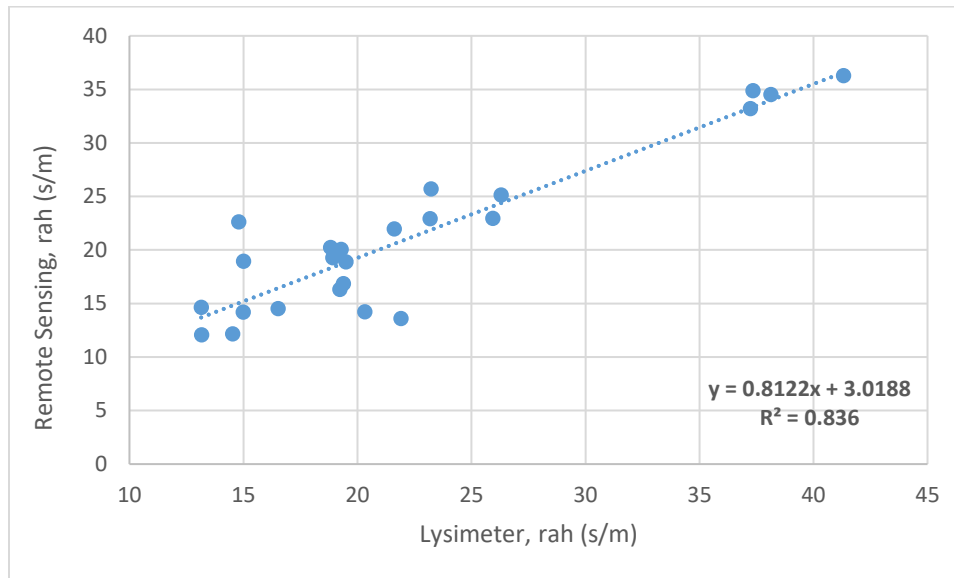


Figure 8. A comparison of Lysimeter-obtained rah values and remote sensing obtained rah values

Below is Table 6 presents rah values obtained from the lysimeter and remote sensing calculations for the given research areas and dates by using the SAT model. According to the Bushland Evapotranspiration and Agricultural Remote Sensing Experiment 2008 (BEAREX08) data, cotton first emerged in two irrigated lysimeters on the east field (fully irrigated) on May 29th, and then on the west field (non-irrigated) on June 13th. Thus, it was expected that a higher canopy height would be estimated for the east part than for the west part for the first evaluation date, which was June 26th. However, the estimated average canopy height values obtained from the west part of the research area were higher than those of the east part for June 26th. The reason for that is the heterogeneity of the non-irrigated part of the research area. Because of the heterogeneity of the surface, the remote sensing-estimated averaged canopy heights for some dates (June 26th, July 12th) were overestimated for the west part of the research area.

When the rah values obtained for each date were analyzed using the lysimeter and remote sensing methods, it could be seen that there was a major difference between the values for NW and SE part of the June 26th. However, the measured wind speed values for lysimeter and remote sensing were close for that date. Lysimeter-obtained rah values were measured as it was expected for the east and west parts of the area, and nearly the same rah values were obtained for the north-east and north-west parts as for the south-east and south-west parts of the research area. The highest rah values were obtained for the date of August 5th, which was the date on which the lowest wind speed values were measured. This resulted in high rah values.

A relatively large difference was also observed between lysimeter- and remote sensing-obtained rah values for the date of August 13th, especially for the NW and SE parts of the research area. Like on June 26th, there was no significant difference between measured wind speed values for the lysimeter and remote sensing methods, and the measured canopy heights were higher for the east part than for the west part of the research area. The only reason for these relative difference between the rah values obtained using remote sensing calculations and those obtained using the lysimeter for the NW part of the research area for August 13th is the heterogeneity of the surface. As was the case for the SE part of the research area, because the rah values were obtained by using a multiple linear regression approach and negative H values were observed on that day, this may have resulted in high rah values from the remote sensing calculations compared to those from the lysimeter.

Table 6. Calculated rah for lysimeter and remote sensing for the given research areas and dates

rah (s/m)					
AREA/DATE	LYSIMETER	REMOTE SENSING	AREA/DATE	LYSIMETER	REMOTE SENSING
NE_JUNE 26	19.49	18.87	NE_JULY 28	18.92	19.26
NW_JUNE 26	15.00	18.93	NW_JULY 28	19.38	16.86
SE_JUNE 26	20.32	14.23	SE_JULY 28	18.82	20.22
SW_JUNE 26	14.99	14.20	SW_JULY 28	19.28	20.03
NE_JULY 12	16.51	14.51	NE_AUGUST 5	41.32	36.26
NW_JULY 12	13.15	14.64	NW_AUGUST 5	37.23	33.19
SE_JULY 12	14.53	12.14	SE_AUGUST 5	38.13	34.52
SW_JULY 12	13.16	12.07	SW_AUGUST 5	37.35	34.86
NE_JULY 20	26.30	25.11	NE_AUGUST 13	19.22	16.32
NW_JULY 20	23.23	25.69	NW_AUGUST 13	21.91	13.60
SE_JULY 20	25.93	22.93	SE_AUGUST 13	14.79	22.62
SW_JULY 20	23.19	22.92	SW_AUGUST 13	21.62	21.97

3.2.2 To Estimation

The air temperature values that were used to compute aerodynamic temperature for the remote sensing calculations were acquired from the weather station that was located near the east lysimeter fields. For the lysimeter air temperature values, the air temperature values from the instrumentations positioned at each large weighing lysimeter were used. Air temperature values were obtained from each large weighing lysimeter, and were the same for both west parts of the lysimeter fields. For the east part of the lysimeter fields, air temperature values were close, with less than 1°C difference. The difference between the temperature values used for the remote sensing and those used for the lysimeter was no larger than 2°C, which made a considerable difference in the estimation of ET_a. In general, the air temperature values used for lysimeter

calculations were higher than the remote sensing air temperature values for all dates except August 5th.

Surface temperature values for lysimeter calculations were acquired from the IRT for each large weighing lysimeter calculations, and from thermal images for remote sensing calculations.

Remote sensing-estimated aerodynamic temperature values were compared with lysimeter-obtained aerodynamic temperature values; this can be seen in Figure 9. As was expected, the surface temperature values of the west part of the lysimeter field, which was managed as a dryland area, were higher than those of the east part of the lysimeter field. This resulted in higher aerodynamic temperature values for the west part of the area.

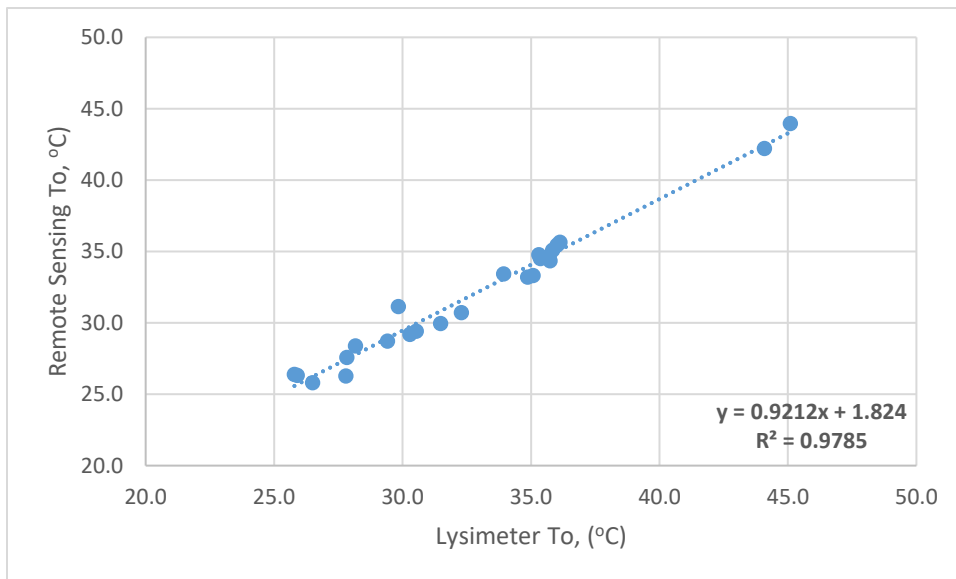


Figure 9. A comparison of lysimeter-obtained To values and remote sensing-obtained To values

As can be seen in Figure 9 and Table 7, the highest aerodynamic temperature values were obtained for the west part of the research area on August 5th. Higher surface aerodynamic resistance values were obtained as well. On August 5th, the IRTs sensed the highest surface temperature values for the west parts, and the highest air temperature values were measured on

that date. Wind speed values were also low (between 2.0 and 2.4 m/s) for that date, which directly resulted in higher surface aerodynamic resistance values. Since the aerodynamic temperature model is a function of air temperature, surface temperature, and surface aerodynamic resistance, the result was the highest aerodynamic temperature values for August 5th.

Table 7. Calculated T_o values for lysimeter and remote sensing for the given research areas and dates

T_o (°C)					
AREA/DATE	LYSIMETER	REMOTE SENSING	AREA/DATE	LYSIMETER	REMOTE SENSING
NE_JUNE 26	36.13	35.64	NE_JULY 28	31.48	29.96
NW_JUNE 26	35.36	34.51	NW_JULY 28	35.30	34.78
SE_JUNE 26	36.01	35.44	SE_JULY 28	30.53	29.42
SW_JUNE 26	35.74	34.36	SW_JULY 28	35.08	33.32
NE_JULY 12	25.90	26.32	NE_AUGUST 5	35.71	34.64
NW_JULY 12	28.17	28.38	NW_AUGUST 5	45.09	43.97
SE_JULY 12	25.79	26.39	SE_AUGUST 5	33.93	33.43
SW_JULY 12	27.83	27.58	SW_AUGUST 5	44.09	42.22
NE_JULY 20	32.28	30.72	NE_AUGUST 13	27.79	26.28
NW_JULY 20	35.83	35.09	NW_AUGUST 13	30.28	29.19
SE_JULY 20	29.83	31.15	SE_AUGUST 13	26.49	25.82
SW_JULY 20	34.87	33.20	SW_AUGUST 13	29.41	28.73

Overall, for most of the dates, remote sensing-estimated T_o values were close to the lysimeter-measured T_o values, with an MBE of 2.33% and an RMSE of 3.33%.

3.2.3 H estimation

Remote sensing-estimated sensible heat flux values that were calculated by using the SAT model were compared with lysimeter “measured” (inverted EB) sensible heat flux. The comparison of the two methods is presented in Figure 10 below. For the first assessment date, June 26th, the obtained H values (Table 8) were similar between the four parts of the research area. Because it was The beginning of the growing season, high H values were expected because of the low ET rate, especially for the west part of the area.

Regarding the aerodynamic temperature values obtained from the two methods on June 26th, the remote sensing-obtained T_o values were slightly higher than the lysimeter-obtained T_o values. The air temperature values used for the remote sensing calculations on June 26th were slightly lower than the lysimeter-measured air temperature as well. In the case of surface aerodynamic resistance, there was a relatively large difference between the lysimeter-measured and remote sensing-estimated r_{ah} values for the NW and SE parts of the research area. Whereas for the NW part of the area, remote sensing-estimated r_{ah} values were higher than the lysimeter-measured r_{ah} values, in the SE part of the research area, the relationship was the reverse. Thus, regarding the remote sensing estimations, lower H values for the NW part and higher H values for the SE part were expected compared to the lysimeter-measured H values. Unsurprisingly, the H values obtained for the NE and SW parts of the research area from remote sensing calculations were similar to the lysimeter-calculated H values, as the r_{ah} values were obtained for the same parts on June 26th.

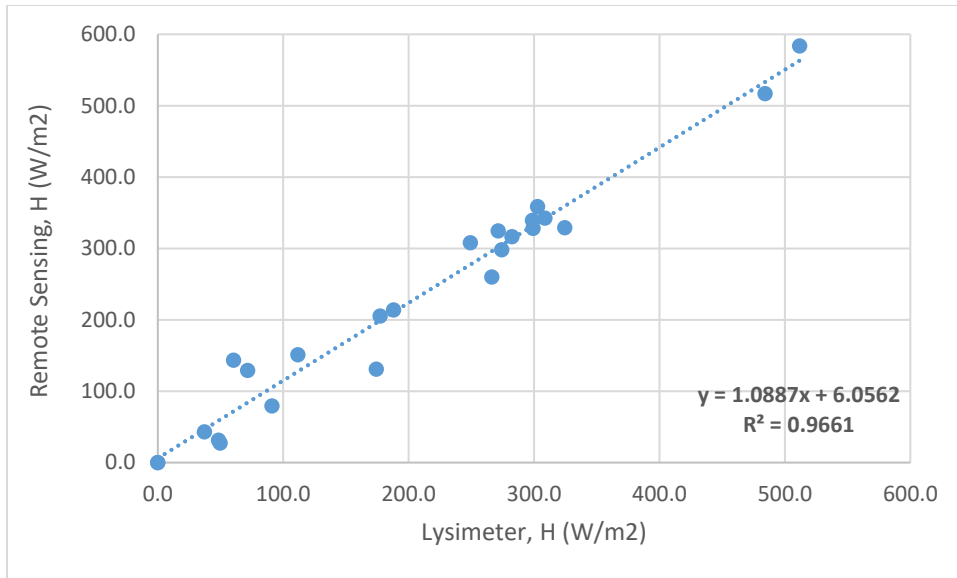


Figure 10. A comparison of lysimeter-obtained H values and remote sensing-obtained H values

Whereas for June 26th the IRTs sensed nearly identical temperatures for all four lysimeter fields, on July 12th there was a large difference between the surface temperature values for the east and west parts of the lysimeter fields. This implies that there was ET on the east side of the research area that decreased the surface temperature. The high temperature resulted in high H values for the west part of the area, as was expected. As can be seen in Figure 10, the highest H values were obtained on that date for both the lysimeter and remote sensing methods. The obtained rah values were small because of the high wind speed on that date. On the other hand, lower H values were expected for July 12th than for June 26th H values for the fully irrigated part of the research area. Figure 8 shows that, besides the NE part of the lysimeter-calculated H values, all other (NE lysimeter, and NE and SE remote sensing) calculated H values for the two methods on that date were higher than those obtained on June 26th.

Table 8. Calculated H values for lysimeter and remote sensing for the given research areas and dates

H (W/m²)					
AREA/DATE	LYSIMETER	REMOTE SENSING	AREA/DATE	LYSIMETER	REMOTE SENSING
NE_JUNE 26	282.25	316.67	NE_JULY 28	48.34	31.30
NW_JUNE 26	298.59	339.35	NW_JULY 28	188.02	214.04
SE_JUNE 26	249.31	307.78	SE_JULY 28	0.00	0.00
SW_JUNE 26	324.34	329.26	SW_JULY 28	177.29	205.19
NE_JULY 12	271.30	324.58	NE_AUGUST 5	91.09	79.33
NW_JULY 12	511.86	583.87	NW_AUGUST 5	302.67	358.50
SE_JULY 12	299.13	328.15	SE_AUGUST 5	37.07	43.03
SW_JULY 12	484.25	517.13	SW_AUGUST 5	274.24	298.13
NE_JULY 20	174.29	131.02	NE_AUGUST 13	49.67	27.48
NW_JULY 20	308.62	342.49	NW_AUGUST 13	111.67	151.02
SE_JULY 20	60.41	143.46	SE_AUGUST 13	0.00	0.00
SW_JULY 20	266.36	260.11	SW_AUGUST 13	71.54	128.98

Because cotton shaded the ground, the H values obtained from remote sensing and lysimeter calculations for July 20th were lower than those obtained on the previous assessment dates. The same situation was observed with remote sensing and lysimeter calculations for both the east and west parts of the research area for July 28th. However, negative H values were obtained for the SE part of the research area on July 28th and August 13th for both the remote sensing and lysimeter calculations. This results show that the SAT model that was used for this study was capable of capturing advection which enhanced the ET process on the well irrigated east fields.

On the other hand, the H values that were obtained for the west part of the research area on August 5th were higher than expected. On that date, the highest To values and relatively high rah values were obtained for the NW and SW parts of the research area for both lysimeter and

remote sensing calculations. Thus, high T_o and ra_h values may have caused high H values for the west part of the area on August 5th. As a result, in most cases, remote sensing-based calculations estimated H to be higher than the lysimeter calculations in Excel. This was mostly because of the air and surface temperature differences between the two methods. As was mentioned above, the T_a values used for the lysimeters calculations were higher than those used for the remote sensing. Therefore, the H values obtained using lysimeter data were lower than the H values obtained using remote sensing, with an MBE of 11.85% and an RMSE of 19.34%.

3.2.4 R_n Estimation

The main objective of this study was to use the same procedure for calculating H , R_n , and G and to obtain ET_a as a residual of these variables for both remote sensing and lysimeter methods. By doing this, it was possible to evaluate the applicability of the T_o model that was used in this study in the research area located in Bushland, Texas by using remote sensing methods. Furthermore, it was possible to compare the accuracy of the remote sensing-obtained ET_a values with the lysimeter-measured ET_a values.

Since most of the variables that were used for the calculation of net radiation for remote sensing and lysimeter were common, it was expected to obtain close R_n values for the two methods, as shown in Figure 11 and Table 9. Air and surface temperature values made minor difference between the two methods when obtaining the R_n values.

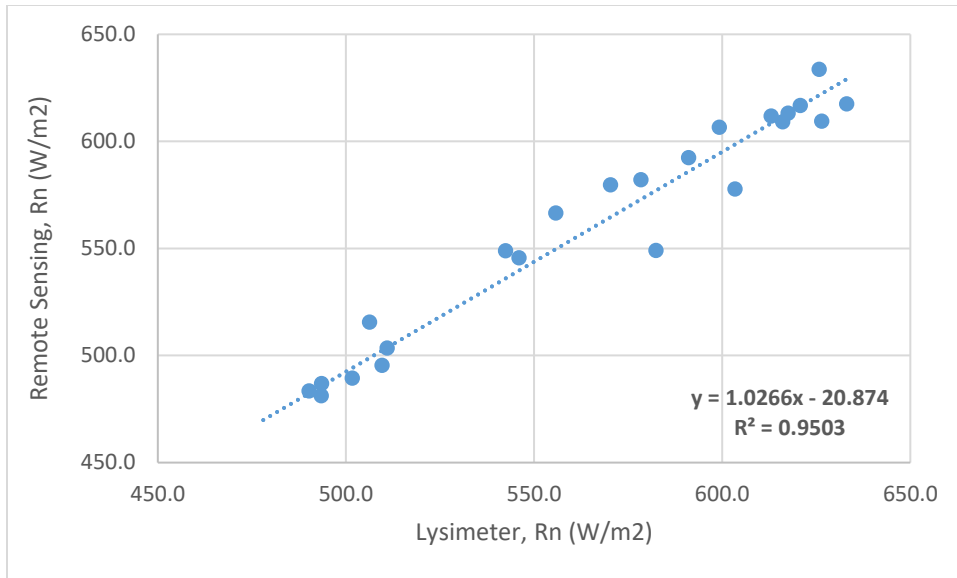


Figure 11. A comparison of lysimeter-obtained Rn values and remote sensing-obtained Rn values

For all dates except August 13th, estimated net radiation values for the east part of the research area were higher than for the west part of the research area. Since the east part was well irrigated, the ET rate was higher than expected and caused the drop in the surface temperature.

Conversely, on August 13th, Rn values of the west part of the research area were slightly higher than the east part Rn values. An examination of the weather data that were obtained on August 13th indicates that the air temperature and surface temperature values measured on that date were highly similar. There was precipitation on that day and this caused a drop in surface temperature, which in turn resulted in close Rn values for all four parts of the research area. For most of the dates, these two systems' estimated net radiation values were close, with an MBE factor of 5.9 W/m² and an RMSE factor of 13.6 W/m².

Table 9. Calculated Rn values with lysimeter and remote sensing for the given research areas and dates

Rn (W/m²)					
AREA/DATE	LYSIMETER	REMOTE SENSING	AREA/DATE	LYSIMETER	REMOTE SENSING
NE_JUNE 26	510.99	503.57	NE_JULY 28	625.73	633.74
NW_JUNE 26	490.20	483.40	NW_JULY 28	545.97	545.58
SE_JUNE 26	501.69	489.40	SE_JULY 28	626.46	609.45
SW_JUNE 26	493.42	481.23	SW_JULY 28	582.43	549.01
NE_JULY 12	613.03	611.84	NE_AUGUST 5	616.05	609.21
NW_JULY 12	542.46	548.99	NW_AUGUST 5	478.01	447.56
SE_JULY 12	620.72	616.80	SE_AUGUST 5	633.10	617.56
SW_JULY 12	555.77	566.53	SW_AUGUST 5	509.62	495.38
NE_JULY 20	570.29	579.77	NE_AUGUST 13	591.09	592.42
NW_JULY 20	493.52	486.98	NW_AUGUST 13	599.21	606.61
SE_JULY 20	603.36	577.80	SE_AUGUST 13	578.40	582.13
SW_JULY 20	506.27	515.56	SW_AUGUST 13	617.49	613.14

3.2.5 G Estimation

As was mentioned in the methodology section, the LAI values used for the calculation of G were obtained from remote sensing calculations, and those values were also used in Excel for the lysimeter calculations. Since the inputs were common for both remote sensing and lysimeter methods, it was expected to obtain close G values for the two methods. Figure 12 presents the G values that were obtained from the lysimeter and remote sensing methods.

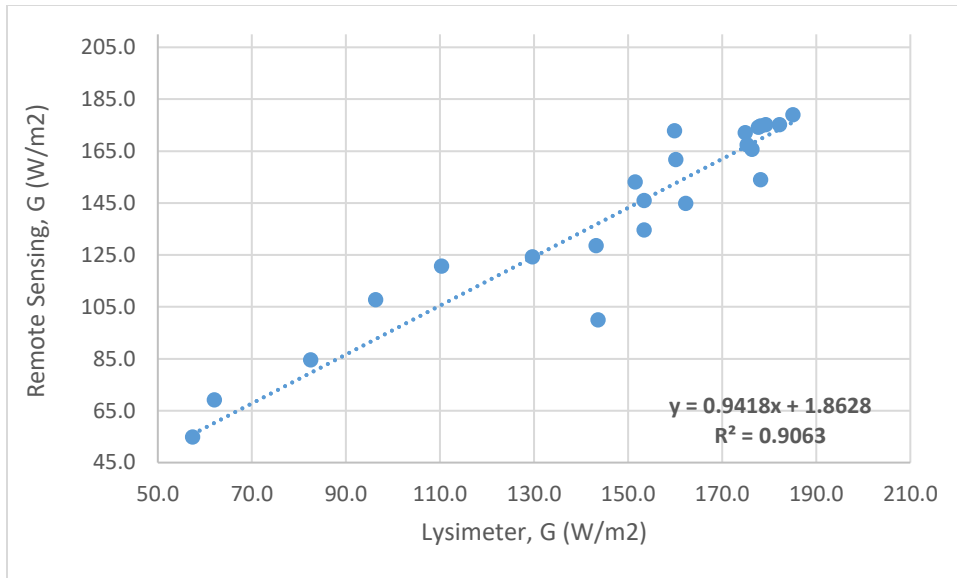


Figure 12. A comparison of lysimeter-obtained G values and remote sensing-obtained G values

While LAI values were small for the west part of the research area, higher G values (Table 10) were obtained for those areas, as was expected. The smallest G values were estimated on the SE part of the research area for August 13th; this area had the highest LAI values and thus canopy heights.

Table 10. Calculated G values with lysimeter and remote sensing for the given research areas and dates

G (W/m ²)					
AREA/DATE	LYSIMETER	REMOTE SENSING	AREA/DATE	LYSIMETER	REMOTE SENSING
NE_JUNE 26	182.17	175.22	NE_JULY 28	96.31	107.69
NW_JUNE 26	177.71	174.19	NW_JULY 28	185.04	179.02
SE_JUNE 26	174.92	172.09	SE_JULY 28	143.57	99.99
SW_JUNE 26	178.16	174.73	SW_JULY 28	178.14	154.04
NE_JULY 12	151.52	153.18	NE_AUGUST 5	82.48	84.54
NW_JULY 12	179.22	175.14	NW_AUGUST 5	162.24	144.82
SE_JULY 12	160.15	161.75	SE_AUGUST 5	61.99	69.11
SW_JULY 12	175.29	167.42	SW_AUGUST 5	143.22	128.59
NE_JULY 20	110.34	120.68	NE_AUGUST 13	57.37	54.84
NW_JULY 20	176.36	165.76	NW_AUGUST 13	159.88	172.84
SE_JULY 20	129.62	124.28	SE_AUGUST 13	66.94	43.60
SW_JULY 20	153.41	146.00	SW_AUGUST 13	153.37	134.57

3.2.6 ET estimation

H values were overestimated with remote sensing calculations for four parts of the research area for June 26th. This in turn caused an underestimation of ET_a values. As was mentioned above, on June 26th higher canopy height values were obtained for the west parts than for the east parts of the area: 0.265 m for north-east part, 0.476 m for north-west part, 0.264 m for south-east part, and 0.475 m for south-west part of the research area. However, obtained LAI values were higher for the east parts than for the west parts of the area on that same date. LAI values were 0.387 m²/m² and 0.366 m²/m² for the north-east and north-west parts of the research area, and 0.416 m²/m² and 0.371 m²/m² for south-east and south-west part of the research area, respectively. Surface aerodynamic resistance values that were obtained with remote sensing calculations for

June 26th were underestimated for the NE, SE, and SW part of the research area; this directly caused overestimation of H. As can be seen in Figure 13, ETa values obtained with remote sensing calculations were underestimated compared to the lysimeter-based ETa calculations. Although no ET rate was obtained for June 26th in the NW and SW parts of the research area with remote sensing calculations, the obtained canopy height values and LAI values indicated that there should have been be ET on this date. For both the NE and SE parts of the research area, an ETa was estimated, and there was more than a 75% difference between the remote sensing calculations and the lysimeter-calculated ETa values.

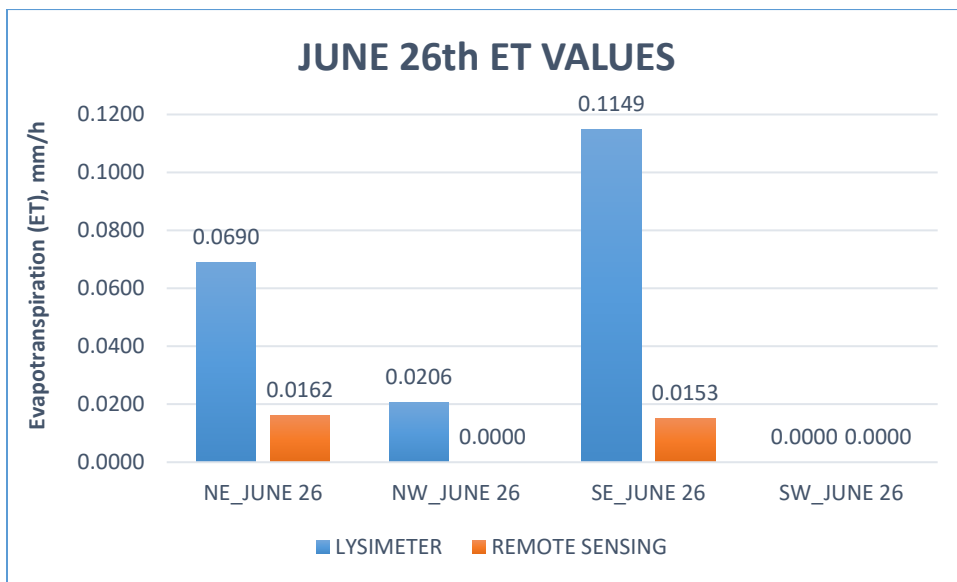


Figure 13. A comparison of lysimeter-obtained ET values and remote sensing-obtained ET values for June 26th

Unlike June 26th, higher canopy height values were obtained for the east part than for west part of the research area on July 12th. Surface aerodynamic resistance values were underestimated with remote sensing calculations in the NE, SE, and SW parts of the research area for July 12th, which caused overestimation of H and underestimation of ETa. Regarding the To values

obtained for July 12th, there is less than 1°C of difference between the lysimeter- and remote sensing-obtained T_o values. Figure 14 presents the ET_a values that were obtained with lysimeter and remote sensing calculations. As was specified above, the highest H values were obtained for the west parts of the area for July 12th, which caused negative LE values to be obtained with both methods based on the energy balance equation for the west parts. This clearly shows that the SAT model that was used in this study was not appropriate for the research area that was chosen. For the NE part of the research area, ET_a was obtained with 32.9% difference and for the SE part of the research area with 23.3% difference with remote sensing-based calculations.

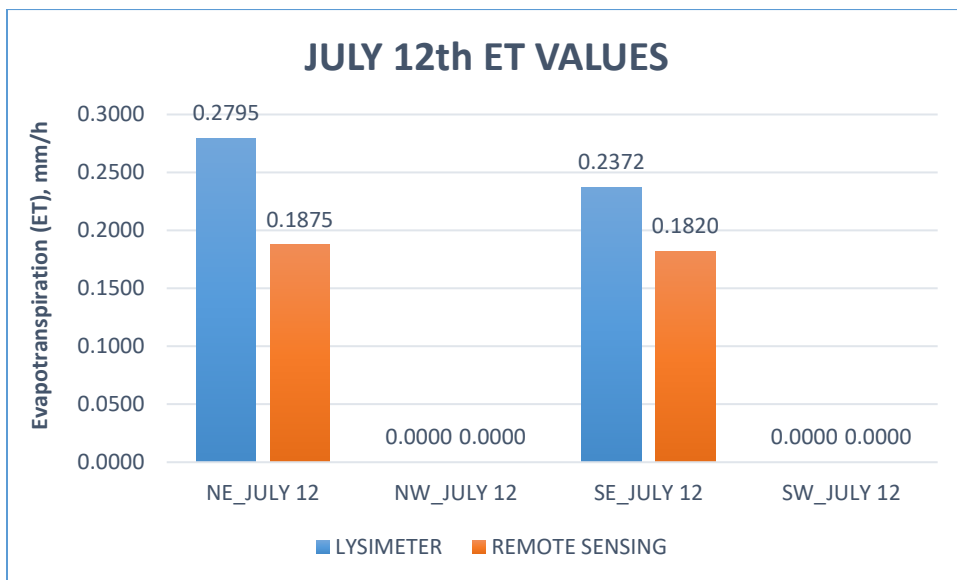


Figure 14. A comparison of lysimeter-obtained ET values and remote sensing-obtained ET values for July 12th

Unlike June 26th and July 12th, on July 20th ET_a values obtained with remote sensing calculations were overestimated when compared with lysimeter-measured ET_a values, except for in the SE part (Figure 15). For the SE part of the research area on July 20th, ra_h was underestimated and T_o was overestimated; thus, H was overestimated with remote sensing calculations. This resulted in a low ET_a value with remote sensing calculations for the SE part of the research area on July

20th. On the other hand, H values were underestimated for the NE and SW parts of the research area, which explains why ETa was overestimated in the NE and SW parts of the area with remote sensing calculations. Although H was overestimated for the NW part of the research area, a high ETa value was estimated with remote sensing calculations compared to the lysimeter ETa value. Because of the heterogeneity of the surface, the components of the sensible heat flux could be overestimated and this resulted in the underestimation of H. The percent differences obtaining ETa for the NE and SE parts of the research area were 14.54 and 25.6, respectively. Eta difference was more than doubled for the NW part of the research area for July 20th. Since the ET rate was too low for that part, small differences had a large impact when calculating ETa with the energy balance equation. For the SW part of the research area, the difference was 39.45 for estimating ETa.

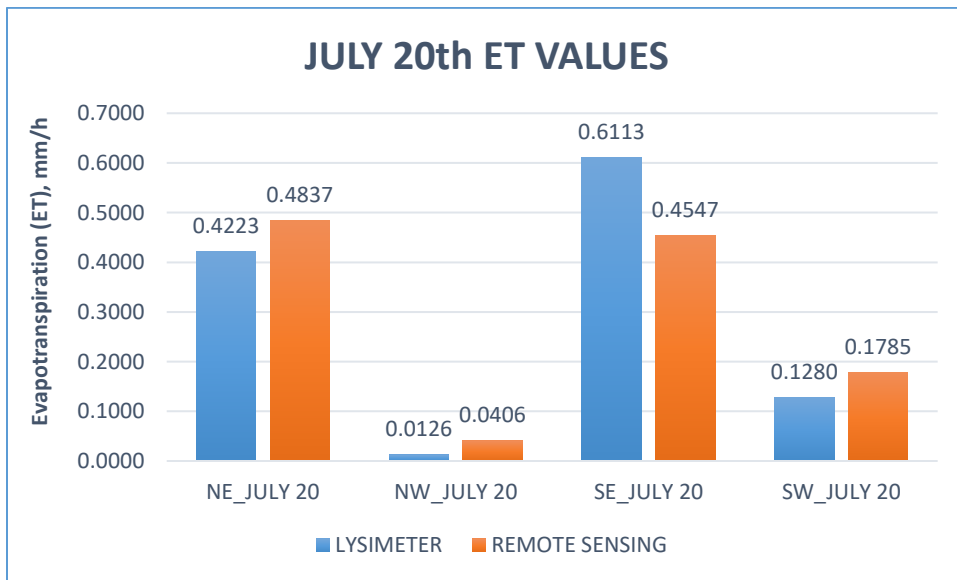


Figure 15. A comparison of lysimeter-obtained ET values and remote sensing-obtained ET values for July 20th

For the NE and SE parts of the research area, the obtained ETa values were overestimated, while for the NW and SW parts, the ETa values were underestimated with remote sensing-based calculations. However, close ETa values were obtained for July 28th with both remote sensing and lysimeter calculations. On the other hand, as was indicated above, for the SE part on July 28th, H was calculated as a negative value for both remote sensing and lysimeter calculations because of the strong advection conditions. H was assumed to be 0 and ETa was calculated by using the energy balance equation as a residual of Rn and G. Rn and G were underestimated for the SE part of the research area for July 28th, which caused overestimation of ETa with remote sensing calculations with a 11.51% difference. Figure shows the magnitude of the ETa values that were obtained for each area with lysimeter and remote sensing calculations on July 28th. ETa was obtained with a 2.87% difference for the NE part of the research area, whereas H was underestimated and caused the overestimation of ETa with remote sensing calculations. Regarding the Eta values that were obtained for the non-irrigated parts, there was a 4% difference for the NW part of the area and an 18.35% difference for the SW part of the area with remote sensing underestimation of ETa values.

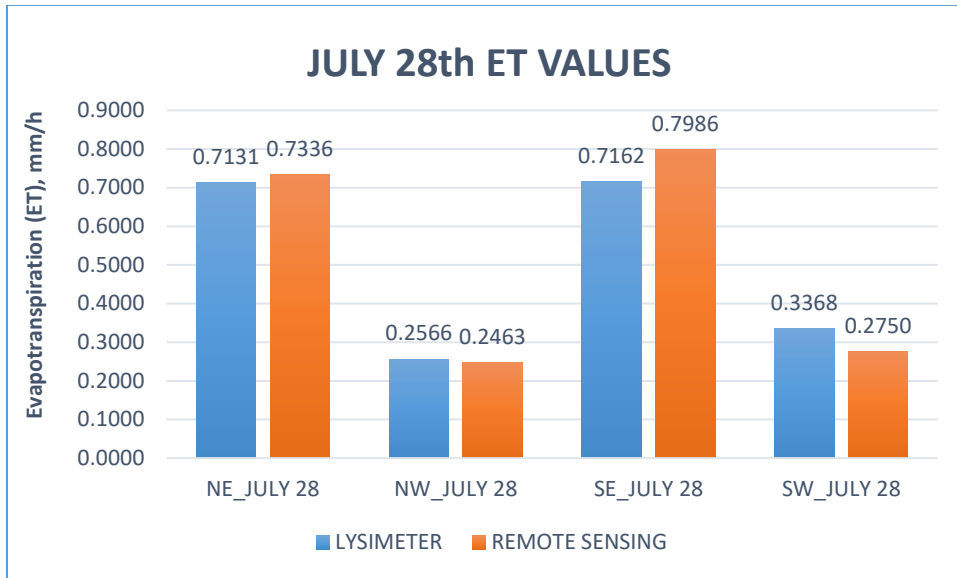


Figure 16. A comparison of lysimeter-obtained ET values and remote sensing-obtained ET values for July 28th

Aerodynamic surface resistance and T_o values were underestimated for four parts of the research area on August 5th with remote sensing calculations. Therefore, overestimation of H and underestimation of E_t were expected. While the results (Figure 17) were as expected for the SE and SW parts of the research area, negative LE values were obtained in the NW part of the research area for both remote sensing and lysimeter calculations of E_t , which was assumed to be 0 as was previously done. On August 5th, the lysimeter measured the highest surface temperature for the NW part of the area, and the highest T_o values for that part were obtained as well. High surface temperature values indicated that the ET rate was low in the NW part of the area. However, the canopy height that was obtained for that part was 0.486 m and the LAI was 0.453 m^2/m^2 , suggesting that there should have been an ET rate in the NW part of the area on August 5th.

Slightly higher E_t values were estimated with remote sensing calculations (1.52% difference) for the NE part of the area on August 5th. Although r_{ah} and T_o were underestimated, H was also

underestimated for the NE part of the area on August 5th. The small difference between the air temperatures on August 5th may have caused the Eta values to be similar for both the lysimeter and remote sensing calculations. The percent differences between the Eta values obtained by remote sensing calculations and those obtained by lysimeter calculations were 5.75 for the SE part and 23.3 for the SW part of the area on this date.

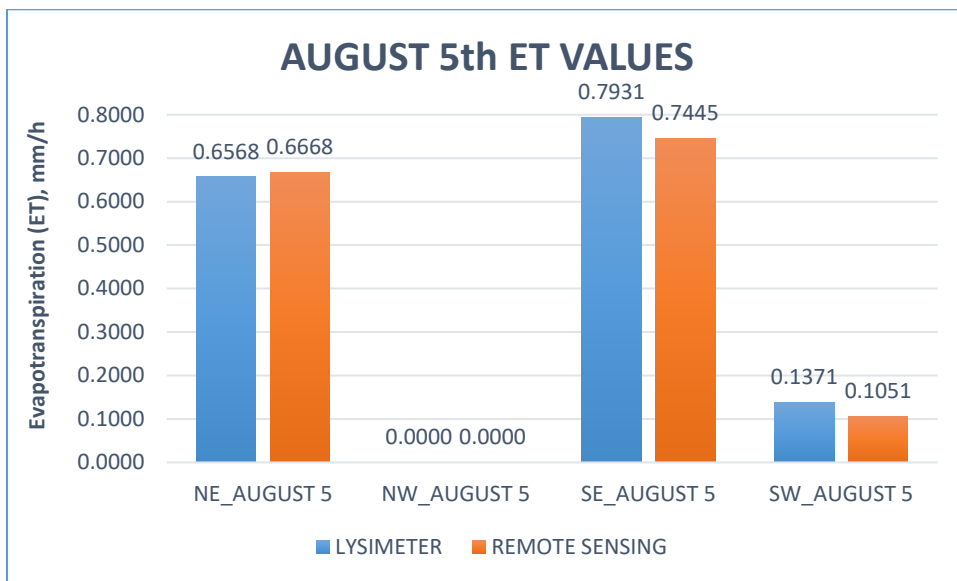


Figure 17. A comparison of lysimeter-obtained ET values and remote sensing-obtained ET values for August 5th

The highest canopy heights and LAI values were obtained on August 13th. As was expected, with cotton shading the ground, the obtained ETa values increased. Using remote sensing calculations, higher ETa values were estimated for the NE and SE parts of the area, and lower ETa values were estimated for the NW and SW parts of the area than by using lysimeter (Figure 18). Regarding the rah and To values that were estimated for the NE part of the area, it can be seen (Table 11, Table 12) that those parameters were underestimated with remote sensing calculations. In addition, there was nearly 1°C of difference between the lysimeter- and remote

sensing-measured air temperatures that were used for the NE part of the research area. The lysimeter-measured air temperature value was higher than the remote sensing-measured air temperature value. r_{ah} , T_o , and T_a parameters caused the underestimation of H with remote sensing calculations, and thus caused an overestimation by 5.61% of the ET_a obtained with the remote sensing system.

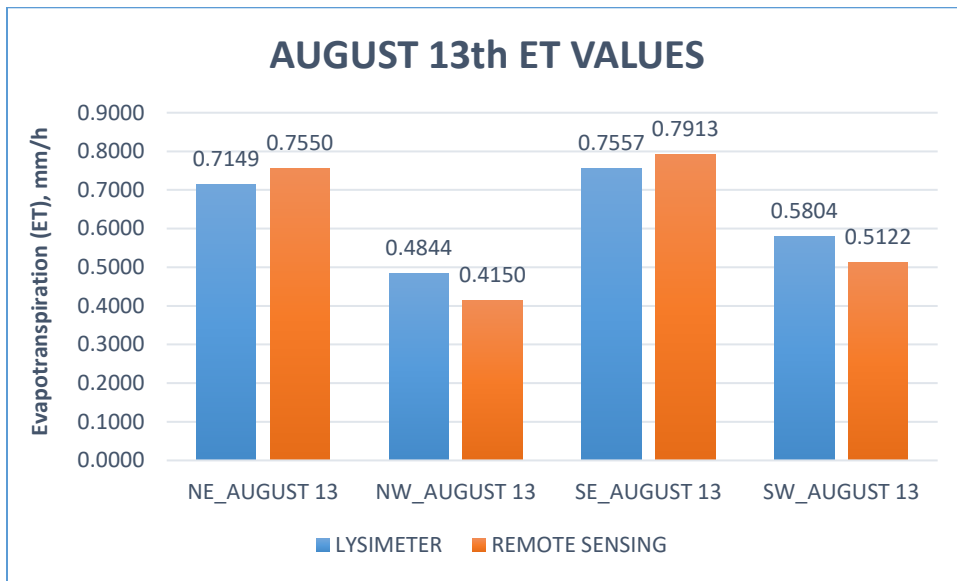


Figure 18. A comparison of lysimeter-obtained ET values and remote sensing-obtained ET values for August 13th

For the SE part of the area, a negative value was obtained for H for both lysimeter and remote sensing calculations, and it was assumed to be 0, as was done before. Since H did not have any effect on the energy balance equation, ET_a was calculated as a residual of R_n and G , which were calculated with common inputs for both the remote sensing and lysimeter methods. The percent difference between the ET_a estimated by those two systems was 4.71, which was higher than expected. R_n was overestimated and G was underestimated with remote sensing calculations, and this caused the overestimation of ET_a with remote sensing. The objective of this study was to calculate H using the SAT model and then obtaining ET_a as a residual from the energy balance

equation; therefore, without any effect of H, the obtained ETa values for the SE part of the research area do not make any sense for the evaluation of model.

As for the NW and SW parts of the research area, H values for August 13th were overestimated with remote sensing calculations, and therefore the ETa values obtained with remote sensing were underestimated. The percent difference was 16.7 for the NW part of the research area, and 11.75 for the SW part of the research area.

Table 11. Lysimeter calculated rah, To, H, Rn, G, and ETa values for the given research areas and dates.

LYSIMETER							
AREA	DATE	rah (s/m)	To (°C)	H (W/m ²)	Rn (W/m ²)	G (W/m ²)	Eta (mm/h)
North-east	26-June	19.49	36.13	282.25	510.99	182.17	0.069
North-west	26-June	15.00	35.36	298.59	490.20	177.71	0.021
South-east	26-June	20.32	36.01	249.31	501.69	174.92	0.115
South-west	26-June	14.99	35.74	324.34	493.42	178.16	0.000
North-east	12-July	16.51	25.90	271.30	613.03	151.52	0.279
North-west	12-July	13.15	28.17	511.86	542.46	179.22	0.000
South-east	12-July	14.53	25.79	299.13	620.72	160.15	0.237
South-west	12-July	13.16	27.83	484.25	555.77	175.29	0.000
North-east	20-July	26.30	32.28	174.29	570.29	110.34	0.422
North-west	20-July	23.23	35.83	308.62	493.52	176.36	0.013
South-east	20-July	25.93	29.83	60.41	603.36	129.62	0.611
South-west	20-July	23.19	34.87	266.36	506.27	153.41	0.128
North-east	28-July	18.92	31.48	48.34	625.73	96.31	0.713
North-west	28-July	19.38	35.30	188.02	545.97	185.04	0.257
South-east	28-July	18.82	30.53	0.00	626.46	143.57	0.716
South-west	28-July	19.28	35.08	177.29	582.43	178.14	0.337
North-east	5-August	41.32	35.71	91.09	616.05	82.48	0.657
North-west	5-August	37.23	45.09	302.67	478.01	162.24	0.000
South-east	5-August	38.13	33.93	37.07	633.10	61.99	0.793
South-west	5-August	37.35	44.09	274.24	509.62	143.22	0.137
North-east	13-August	19.22	27.79	49.67	591.09	57.37	0.715
North-west	13-August	21.91	30.28	111.67	599.21	159.88	0.484
South-east	13-August	14.79	26.49	0.00	578.40	66.94	0.756
South-west	13-August	21.62	29.41	71.54	617.49	153.37	0.580

Table 12. Remote Sensing obtained rah, To, H, Rn, G and ET values for the given research areas and dates.

REMOTE SENSING							
AREA	DATE	rah (s/m)	To (°C)	H (W/m ²)	Rn (W/m ²)	G (W/m ²)	ET (mm/h)
North-east	26-June	18.87	35.64	316.67	503.57	175.22	0.016
North-west	26-June	18.93	34.51	339.35	483.40	174.19	0.000
South-east	26-June	14.23	35.44	307.78	489.40	172.09	0.015
South-west	26-June	14.20	34.36	329.26	481.23	174.73	0.000
North-east	12-July	14.51	26.32	324.58	611.84	153.18	0.187
North-west	12-July	14.64	28.38	583.87	548.99	175.14	0.000
South-east	12-July	12.14	26.39	328.15	616.80	161.75	0.182
South-west	12-July	12.07	27.58	517.13	566.53	167.42	0.000
North-east	20-July	25.11	30.72	131.02	579.77	120.68	0.484
North-west	20-July	25.69	35.09	342.49	486.98	165.76	0.041
South-east	20-July	22.93	31.15	143.46	577.80	124.28	0.455
South-west	20-July	22.92	33.20	260.11	515.56	146.00	0.179
North-east	28-July	19.26	29.96	31.30	633.74	107.69	0.734
North-west	28-July	16.86	34.78	214.04	545.58	179.02	0.246
South-east	28-July	20.22	29.42	0.00	609.45	99.99	0.799
South-west	28-July	20.03	33.32	205.19	549.01	154.04	0.275
North-east	5-August	36.26	34.64	79.33	609.21	84.54	0.667
North-west	5-August	33.19	43.97	358.50	447.56	144.82	0.000
South-east	5-August	34.52	33.43	43.03	617.56	69.11	0.744
South-west	5-August	34.86	42.22	298.13	495.38	128.59	0.105
North-east	13-August	16.32	26.28	27.48	592.42	54.84	0.755
North-west	13-August	13.60	29.19	151.02	606.61	172.84	0.415
South-east	13-August	22.62	25.82	0.00	582.13	43.60	0.791
South-west	13-August	21.97	28.73	128.98	613.14	134.57	0.512

Below, Table 13 presents the daily ET values obtained from the lysimeter and remote sensing calculations for the date were assessed. The daily values of ET ranged from 0.30 mm/d to 19.17 mm/d. For some dates measured and observed, the daily ET values were assumed to be 0, as was explained before. The lowest daily ET value was measured using the lysimeter method for the north-west part on July 20th, while the highest daily ET value was observed with remote sensing-based calculations on July 28th for the south-east part of the research area.

Table 13. Daily ET values obtained from the lysimeter and remote sensing methods

AREA	DATE	ET (mm/d)	
		LYSIMETER	REMOTE SENSING
North-east	26-June	1.66	0.39
North-west	26-June	0.49	0.00
South-east	26-June	2.76	0.37
South-west	26-June	0.00	0.00
North-east	12-July	6.71	4.50
North-west	12-July	0.00	0.00
South-east	12-July	5.69	4.37
South-west	12-July	0.00	0.00
North-east	20-July	10.13	11.61
North-west	20-July	0.30	0.98
South-east	20-July	14.67	10.91
South-west	20-July	3.07	4.28
North-east	28-July	17.11	17.61
North-west	28-July	6.16	5.91
South-east	28-July	17.19	19.17
South-west	28-July	8.08	6.60
North-east	5-August	15.76	16.00
North-west	5-August	0.00	0.00
South-east	5-August	19.03	17.87
South-west	5-August	3.29	2.52
North-east	13-August	17.16	18.12
North-west	13-August	11.63	9.96
South-east	13-August	18.14	18.99
South-west	13-August	13.93	12.29

When estimating the actual ET with remote sensing system compared to measuring the actual ET values with lysimeters, the MBE was 2.67% and the RMSE was 8.61% for the overall system.

3.3 CWSI Assessment

While CWSI rates of 0.94 were obtained for the NE and SE parts of the research area with remote sensing calculations on June 26th, CWSI rates of 0.75 and 0.58 were obtained for the NE and SE parts of the research area, respectively, with lysimeter calculations (Table 14). The ET rate was low on June 26th because it was beginning of the growing season. Therefore, a high CWSI rate was expected for the east part of the area on that date. There was relatively large difference between the CWSI rates obtained with lysimeter calculations and remote sensing calculations (Figure 19) in the SE part of the research area on June 26th, due to the large ET difference on that date.

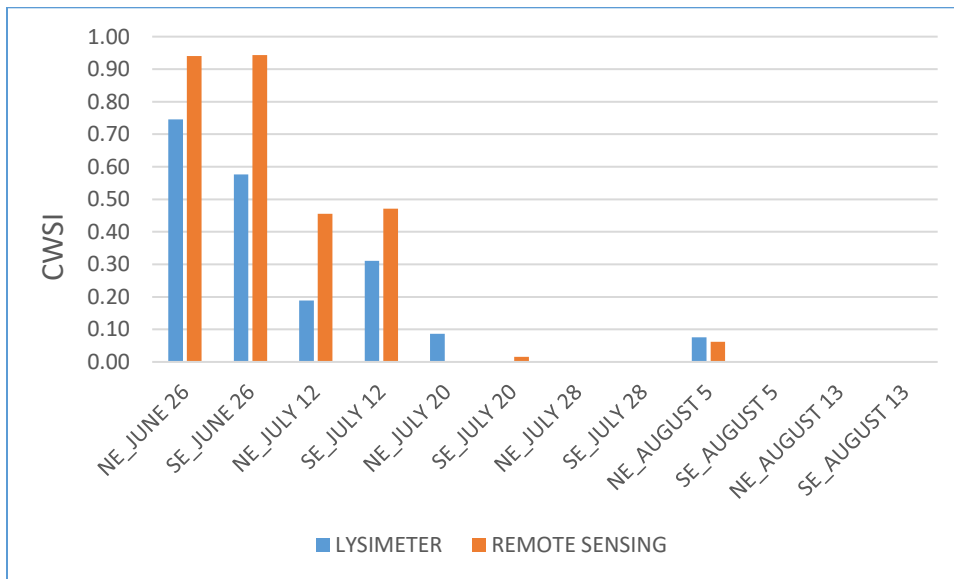


Figure 19. A CWSI comparison for east part of the research area

When the CWSI rates are analyzed for the east part of the research area on July 12th, it can be seen that (Table 14, Figure 19) the CWSI rates decreased with time, which was an expected result. Like the rates on June 26th, the rates obtained on July 12th for the NE and SE parts of the research area were nearly the same with remote sensing calculations. However, there was a large difference between the NE and SE parts of the research area with regard to the lysimeter-calculated CWSI results.

Table 14. Obtained CWSI values with lysimeter and remote sensing calculations for east part of the research area

AREA	LYSIMETER	REMOTE SENSING
NE_JUNE 26	0.75	0.94
SE_JUNE 26	0.58	0.94
NE_JULY 12	0.19	0.46
SE_JULY 12	0.31	0.47
NE_JULY 20	0.09	0.00
SE_JULY 20	0.00	0.02
NE_JULY 28	0.00	0.00
SE_JULY 28	0.00	0.00
NE_AUGUST 5	0.08	0.06
SE_AUGUST 5	0.00	0.00
NE_AUGUST 13	0.00	0.00
SE_AUGUST 13	0.00	0.00

Since the west part was a well-irrigated area and with crops shading the ground, the obtained ET rate increased, and this led to low ET rates for the west part of the research area for other assessment dates (July 20th, July 28th, August 5th, and August 13th). For most of the dates, the CWSI rate was obtained as 0 or close to 0 with both lysimeter and remote sensing calculations. The calculated MBE value of the obtained CWSI rate for the west part of the research area was 0.89%, and the RMSE value was 6%.

As was previously mentioned, the east part of the research area was the non-irrigated part, and therefore the obtained ET values were low for most of the dates in this area. The obtained CWSI values on June 26th for the NE part were 0.92 with lysimeter calculations and 1.0 with remote sensing calculations. There was precipitation on June 26th, which caused an ET rate on that date. Regarding the NE and SE parts of the research area on July 12th, it can be seen (Figure 20, Table 15) that lysimeter- and remote sensing-obtained CWSI rates were 1.0 for both parts.

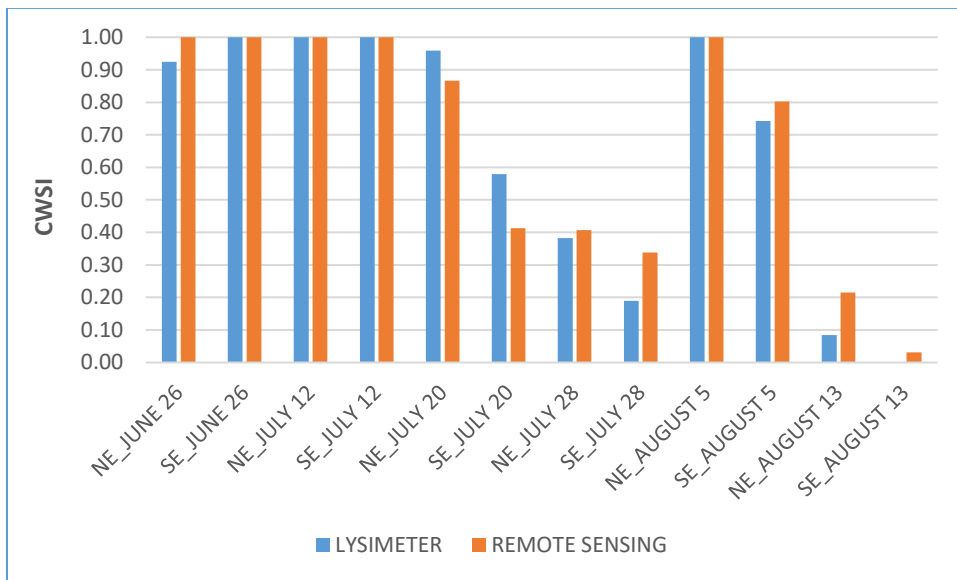


Figure 20. A CWSI comparison for west part of the research area

CWSI rates gradually decreased (Figure 22) over time except in the NE and SE parts of the research area on August 5th. Regarding the ET rates that were obtained on that date for the east part, it can be seen that the obtained ET values for the NE part of the research area were 0 with both lysimeter and remote sensing calculations. Therefore, the CWSI rate was 1.0. The obtained ET rates were low for the SE part of the area on August 5th as well, which resulted in high CWSI rates.

Table 15. Obtained CWSI values with lysimeter and remote sensing calculations for west part of the research area

AREA	LYSIMETER	REMOTE SENSING
NE_JUNE 26	0.92	1.00
SE_JUNE 26	1.00	1.00
NE_JULY 12	1.00	1.00
SE_JULY 12	1.00	1.00
NE_JULY 20	0.96	0.87
SE_JULY 20	0.58	0.41
NE_JULY 28	0.38	0.41
SE_JULY 28	0.19	0.34
NE_AUGUST 5	1.00	1.00
SE_AUGUST 5	0.74	0.80
NE_AUGUST 13	0.08	0.22
SE_AUGUST 13	0.00	0.03

Precipitation was monitored on August 13th. Even the east part of the research area was under stress conditions: high ET rates were measured with lysimeters and calculated with remote sensing. The high ET rates on August 5th were caused by the drop in plant temperature; consequently, the CWSI rates were low on this date. In conclusion, the obtained MBE was 3.77% and the RMSE was 10.76% for the east part of the research area. When comparing the obtained MBE and RMSE values for the east part with the MBE and RMSE values for the west part, it can clearly be seen that the CWSI method worked better for the west part of the research area.

CHAPTER 4: CONCLUSION

This study compared ETa results that were obtained from multispectral airborne remote sensing data with ETa measured with large weighing lysimeters situated in the center of each field (NE, NW, SE, and SW). Then, ETa calculated with remote sensing data compared with ETa calculated by large weighing lysimeters data in MS Excel. This was done with the SAT model that was empirically calibrated by Chávez in 2010 using heat flux towers. H was estimated by using the SAT model, and then ET was calculated as a residual of e energy balance algorithm. ETa hourly (mm/h) and daily (mm/d) results obtained using the remote sensing system were compared with ETa results obtained with large weighing lysimeters measurements and calculations.

The SAT model applied by using airborne multispectral imagery and weather station data resulted in larger ETa (mm/h and mm/d) errors especially in the beginning of the growing season for both east and west part of the research area. Comparison of ET results that were obtained from multispectral airborne remote sensing data by using SAT model with ET measured by mass balance using large weighing lysimeters showed 25.9% MBE and 44.07% RMSE for east part of the research area and 42.13% MBE and 42.91% RMSE for west part of the research area. The SAT model overestimated the actual ET values with a high differences in the beginning of the growing season because of the small hc and LAI. However, with cotton shades the ground the SAT model gets better for estimating actual ET values.

On the other hand, it was examined the difference between hc and LAI for both remote sensing calculations and lysimeter measurements. Remote sensing obtained hc and LAI values higher than lysimeter measured values which caused overestimation of actual ET with remote sensing

calculations. Additionally, the SAT model that was used in this study is dependent on LAI when calculating h_c and with h_c calculating r_{ah} . For the low crop density or sparse vegetation conditions, remote sensing estimation of LAI and h_c might be overestimated which directly affect the performance of SAT model.

The primary purpose of using the SAT model for this study was to use T_o instead of T_s which is generally larger than T_o for heterogeneous surfaces and which may thus cause overestimation of H and underestimation of ET. Therefore, the applicability of the SAT model was tested for the research area that was located in Bushland, Texas for six days of the years in which airborne remote sensing data were collected. The actual ET results obtained with using SAT model compared with actual ET calculated with T_s in MS Excel with large weighing lysimeters data. Obtained H values were very high, especially for NW and SW part of the research area, which caused underestimation of actual ET calculated with T_s . On the other hand, another T_o model was applied which is function of T_a , T_s , LAI and u . Accounting LAI and u in the T_o model worked better than T_o model that was used in this study in the beginning of the growing season. Then, both T_o model performed nearly same for estimating actual ET for the remaining growing period.

As was previously mentioned, T_o and T_s values are close for homogeneous surfaces conditions. Therefore, the results that were obtained from the west part of the research area, which was under a dryland regime, had major importance for testing the applicability of the SAT model. However, for this case, beyond the lack of irrigation, the west fields displayed sparse vegetation conditions and heterogeneity due to external factors (chemical residual). While for the irrigated fields, SAT can be better tested for the different crop growth periods (different LAI, h_c , and vegetation percent cover conditions). For this research, both east and west part obtained H values

with remote sensing calculations higher than lysimeter measured H values, which caused underestimation of ET with remote sensing calculations with an MBE of 2.67% and an RMSE of 8.61%.

Potential crop ET was calculated by using REF-ET software and tabulated Kc values, which varies with the crop stage growth. Then, CWSI was computed with actual ET values from the SAT model that were obtained from remote sensing data and then evaluated with lysimeters's data.

The CWSI ranges were calculated with an actual ET values that were obtained from remote sensing and lysimeter calculations, and potential ET values that were obtained with a REF-ET calculator and Kc. The calculated MBE and RMSE values of the obtained CWSI rate were 0.89% and 6%, respectively, for the west part of the research area, and 3.77% and 10.76%, respectively, for the east part of the research area. Computing crop water stress using ETa from SAT and then reverting to ETa using ETp it seems to improve the ET estimation due to better assimilation of advection by the ETp or ETreference method.

The incomplete canopy cover was monitored in the west part of the research area, which was under water stress throughout the entire cotton-growing period. High temperature differences caused the limitation of application of the SAT and CWSI methods to the west area. The SAT model performed well for the east part of the research area, which was well irrigated. However, the model requires some improvement with regard to water stress conditions. The CSWI method performed better than the SAT model, especially for the non-irrigated part of the research area.

REFERENCES

- Allen, R.G., L.S. Pereira, and M. Smith. 1998. Crop evapotranspiration: Guidelines for computing crop water requirements. United Nations Food and Agriculture Organization, Irrigation and Drainage Paper 56, Rome, Italy, 300.
- Allen, R.G. W. Bastiaanssen, J. Wright, A. Morse, M. Tasumi and R Trezza. 2002. "Evapotranspiration from satellite images for water management and hydrologic balances," Proceedings of 18th International Congress on Irrigation and Drainage: July 2002, Montreal, Canada.
- Allen, R. G., M. Tasumi, and R. Trezza. 2007. Satellite-based energy balance for mapping evapotranspiration with internalized calibration (METRIC): Model. ASCE J. Irrig. And Drain. Eng. 133(4): 380-394.
- ASCE-EWRI. (2005). the ASCE Standardized Reference Evapotranspiration Equation. Report 07844-0805-X, ASCE Task Committee on Standardization of Reference Evapotranspiration. Reston, Va.: American Society of Civil Engineers
- Bastiaanssen, W.G.M. 1998. Remote Sensing in Water Resources Management: The State of the Art, IWMI, Sri Lanka.
- Bastiaanse, W.G.M., R.A.L. Brito, M.G. Bos, R.A. Souza, E.B. Cavalcanti and M.M. Bakker. 2001. Low cost satellite data for monthly irrigation performance monitoring: benchmarks from Nilo Coelho, Brazil. Irrigation and Drainage Systems 15:53-79.
- Bouleta, G, A. Oliosob, E. Ceschiaa, O. Marloieb, B. Couderta, V. Rivallanda, J. Chirouzea, G. Chehbounia (2012). An empirical expression to relate aerodynamic and surface temperatures for use within single-source energy balance models. Agricultural and Forest Meteorology 161 (2012) 148– 155.
- Brutsaert, W. 1975. On a derivable formula for long-wave radiation from clear skies. Water Resour. Res. 11(5): 742-744.
- Brutsaert, W. 1982. Evaporation into the Atmosphere. Theory, History, and Applications. Boston, Mass.: D. Reidel.
- Businger, J. A. 1988. A note on the Businger-Dyer profiles. Boundary-Layer Meteorol. 42(1-2): 145-151
- Chávez, J., Neale, C. M. U., Hipps, L. E., Prueger, J. H., & Kustas, W. P. (2005). Comparing Aircraft-Based Remotely Sensed Energy Balance Fluxes with Eddy Covariance Tower Data Using Heat Flux Source Area Functions. Journal of Hydrometeorology, 6(6), 923–940. doi:10.1175/JHM467.1
- Chávez, J.L., T.A. Howell, P.H. Gowda, K.S. Copeland, and J.H. Prueger. 2010. Surface Aerodynamic Temperature Modeling over Rainfed Cotton. Transactions of the ASABE, 53(3):759-767.

- Chehbouni, A., D. Lo Seen, E. G. Njoku, and B. M. Monteny. 1996. Examination of the difference between radiative and aerodynamic surface temperature over sparsely vegetated surfaces. *Remote Sensing Environ.* 58(2): 177-186.
- Choudhury, B. J., R. J. Reginato, and S. B. Idso. 1986. An analysis of infrared temperature observations over wheat and calculation of latent heat flux. *Agric. Forest Meteorol.* 37(1): 75-88.
- Crago, R., Friedl, M., Kustas, W., Wang, Y. (2004) Investigation of aerodynamic and radiometric land surface temperatures. NASA Scientific and Technical Aerospace Reports (STAR) 42(1)
- DeJonge, K. C., Taghvaeian, S., Trout, T. J., & Comas, L. H. (2015). Comparison of canopy temperature-based water stress indices for maize. *Agricultural Water Management*, 156, 51-62.
- Doorenbos, J. and W.O. Pruitt. 1977. Crop water requirements, Rome, Italy.
- Dyer, A. J., and B. B. Hicks. 1970. Flux-gradient relationship in the constant flux layer. *Quart. J. Royal Meteorol. Soc.* 96(410): 715-721.
- Dyer, A. J. 1974. A review of flux-profile relationships. *Boundary-Layer Meteorol.* 7(3): 363-372.
- Evet, S.R., Kustas, W.P., Gowda, P.H., Anderson, M.C., Prueger, J.H., Howell, T.A, 2012. Overview of the Bushland evapotranspiration and agricultural remote sensing experiment 2008 (BEAREX08): A field experiment evaluating methods for quantifying ET at multiple scales, *Advances in water resources*, 50 (2012) 4-19.
- Gardner, B. R., (1979). Plant and canopy temperatures in corn as influenced by differential moisture stress. M.Sc. Thesis, University of Nebraska, 119 pp.
- Gowda, P. H., J. L. Chavez, P. D. Colaizzi, S. R. Evett, T. A. Howell, and J. A. Tolk. 2008. ET mapping for agricultural water management: Present status and challenges. *Irrig. Sci.* 26(3): 223-237.
- Hoffman, G. J., R. G. Evans, M. E. Jensen, D. L. Martin, and R. L. Elliott. (2007b). Design and Operation of Farm Irrigation Systems. 2nd ed. American Society of Agricultural and Biological Engineers. (2007): 211-215.
- Howell, Terry A., Scnehider Arland D., Jensen Marvin E. History of lysimeter design and use for evapotranspiration measurements.
- Idso, S. B., stomatal regulation of evaporation from well-watered plant canopies; A new synthesis. *Agr Meteorol* 29; 217.
- Idso, S.B., Reginato, R.J., Jackson, R.D., and Pinter Jr., P. J., (1981a). Measuring yield-reducing plant water potential depressions in wheat by infrared thermometry. *Irrigation Sc* 2; 205-212.
- Idso, S.B., Reginato, R.J., and Farah, S. M., (1982). Soil and atmosphere induced plant water stress in cotton as inferred from foliage temperatures. *Water Resources Res* 18; 1143-1148.
- Jackson, R.D., Reginato, R.J., and Idso, S.B. (1977), Wheat canopy temperature: A practical tool for evaluating water requirements. *Water Resources Res* 13; 651-656.

- Jackson, R. D., Idso, S. B., Reginato, R. J., & Pinter, P. J. (1981). Canopy temperature as a crop water stress indicator. *Water resources research*, 17(4), 1133-1138.
- Kirkham, M. B., (2005). "Principles of soil and plant water relations", Stress-degree day concept and crop-water stress index, pg. 437-453.
- Kustas, W. P., & Norman, J. M. (1996). Use of remote sensing for evapotranspiration monitoring over land surfaces. *Hydrological Sciences Journal-Journal Des Sciences Hydrologiques*, 41(4), 495–516.
- Lillesand, Kiefer, Chipman (2007). *Remote sensing and image interpretation*, sixth edition.
- Mahan, J.R. and Yeater, K.M. (2008) *Agricultural Applications of a Low-Cost Infrared Thermometer*. *Computers and Electronics in Agriculture*, 64, 262-267.
- Mahan James R., Burke John J., (2015) "Active management of plant canopy temperature as a tool for modifying plant metabolic activity" *American Journal of Plant Sciences*, 2015, 6, 249-259.
- Norman, J. M., Kustas, W. P., & Humes, K. S. (1995). Source approach for estimating soil and vegetation energy fluxes in observations of directional radiometric surface temperature. *Agricultural and Forest Meteorology*, 77(3-4), 263–293.
- Sugita, M., and W. Brutsaert. 1990. Regional surface fluxes from remotely sensed surface skin temperature and lower boundary layer measurements. *Water Resour. Res.* 26(12): 2937-2944.
- Suleiman, A., & Crago, R. (2002). Analytical land atmosphere radiometer model (ALARM) applied to a dense canopy. *Agricultural and Forest Meteorology*, 112, 151–159.
- Trezza, R. (2002). "Evapotranspiration using a satellite-based surface energy balance with standardized ground control." PhD thesis, Dept., Biological and Irrigation Engineering, Utah State Univ.
- Walker, G. K., (1980). Relation between crop temperature and the growth and yield of kidney beans (*Phaseolus vulgaris* L.). PhD thesis, University of California, Davis, CA, 203pp.
- Webb, E. K. 1970. Profile relationships: The log-linear range, and extension to strong stability. *Quart. J. Royal Meteorol. Soc.* 96(407): 67-90.
- Wright, J.L. 1982. New evapotranspiration crop coefficients. *Journal of Irrigation and Drainage* 108:57-74.

APPENDIX A

The ASCE-EWRI (2005) standardized Penman-Monteith (PM) method has the form:

$$ET_{sz} = \frac{0.408\Delta(R_n - G) + \gamma \frac{C_n}{T + 273} u_2 (e_s - e_a)}{\Delta + \gamma(1 + C_d u_2)} \quad (A.1)$$

Where; ET_{sz} is standardized reference crop evapotranspiration for short and tall surfaces (mm d^{-1} for daily time steps or mm h^{-1} for hourly time steps), R_n is calculated net radiation at the crop surface ($\text{MJ m}^{-2} \text{d}^{-1}$ for daily time steps or $\text{MJ m}^{-2} \text{hr}^{-1}$ for hourly time steps), G is soil heat flux density at the soil surface ($\text{MJ m}^{-2} \text{d}^{-1}$ for daily time steps or $\text{MJ m}^{-2} \text{hr}^{-1}$ for hourly time steps), T is mean daily or hourly temperature at 1.5 to 2.5 m height ($^{\circ}\text{C}$), u_2 is mean daily or hourly wind speed at 2 m height (m s^{-1}), e_s is saturation vapor pressure at 1.5 to 2.5 m height (kPa), calculated for daily time steps as the average of saturation vapor pressure at maximum and minimum temperature, e_a is mean actual vapor pressure at 1.5 to 2.5 m height (kPa), Δ is slope of the saturation vapor pressure-temperature curve ($\text{kPa } ^{\circ}\text{C}^{-1}$), γ is psychrometric constant ($\text{kPa } ^{\circ}\text{C}^{-1}$), C_n is numerator constant that changes with reference type and calculation time step, C_d is denominator constant that changes with reference type and calculation time step.

C_n and C_d were obtained from simplifying many terms in the ASCE-EWRI (2005) standardized PM equation. C_n values take account for time step and aerodynamic roughness of the surface and C_d values take account for time step, bulk surface resistance, and aerodynamic roughness of the surface.

$$\gamma = 0.000665P \quad (\text{A.2})$$

Where; γ is psychrometric constant ($\text{kPa } ^\circ\text{C}^{-1}$), P is mean atmospheric pressure at station elevation z , (kPa).

$$\Delta = \frac{2503 \exp\left(\frac{17.27T}{T + 237.3}\right)}{(T + 237.3)^2} \quad (\text{A.3})$$

Where; Δ is slope of the saturation vapor pressure-temperature curve ($\text{kPa } ^\circ\text{C}^{-1}$), T is mean air temperature ($^\circ\text{C}$).

$$e^o(T) = 0.6108 \exp\left(\frac{17.27T}{T + 237.3}\right) \quad (\text{A.4})$$

Where; e_s is saturation vapor pressure (kPa), $e^o(T)$ is saturation vapor pressure function (kPa), T is average hourly air temperature ($^\circ\text{C}$).

$$e_a = \left(\frac{RH}{100}\right) e_s \quad (\text{A.5})$$

Where; e_a is actual vapor pressure (kPa), e_s is saturation vapor pressure (kPa), RH is hourly

$$R_n = R_{ns} - R_{nl} \quad (\text{A.6})$$

Where; R_{ns} is net short-wave radiation ($\text{MJ m}^{-2} \text{h}^{-1}$), defined as being positive downwards and negative upwards, R_{nl} is net outgoing long-wave radiation ($\text{MJ m}^{-2} \text{h}^{-1}$), defined as being positive upwards and negative toward the surface.

$$R_{ns} = R_s - \alpha R_s = (1 - \alpha)R_s \quad (\text{A.7})$$

Where; R_{ns} is net solar or short-wave radiation ($\text{MJ m}^{-2} \text{h}^{-1}$), α is albedo or canopy reflection coefficient, is fixed at 0.23 for the standardized short and tall reference surfaces (dimensionless), R_s is incoming solar radiation ($\text{MJ m}^{-2} \text{h}^{-1}$).

$$R_{nl} = R_{lu} - R_{ld} \quad (\text{A.8})$$

$$\text{daily } R_{nl} = \sigma f_{cd} (0.34 - 0.14 \sqrt{e_a}) \left(\frac{T_{Kmax}^4 + T_{Kmin}^4}{2} \right) \quad (\text{A.9})$$

And for hourly R_{nl} is:

$$\text{hourly } R_{nl} = \sigma f_{cd} (0.34 - 0.14 \sqrt{e_a}) T_{Khr}^4 \quad (\text{A.10})$$

Where; R_{nl} is net outgoing long-wave radiation ($\text{MJ m}^{-2} \text{d}^{-1}$ or $\text{MJ m}^{-2} \text{h}^{-1}$), σ is Stefan-Boltzmann constant ($4.901 \times 10^{-9} \text{ MJ K}^{-4} \text{m}^{-2} \text{d}^{-1}$ or $2.042 \times 10^{-10} \text{ MJ K}^{-4} \text{m}^{-2} \text{h}^{-1}$), f_{cd} is a cloudiness function (dimensionless) and limited to $0.05 < f_{cd} < 1.0$, e_a is a cloudiness function (dimensionless) and limited to $0.05 < f_{cd} < 1.0$, T_{Kmax} is maximum absolute temperature during the 24-hour period (K), T_{Kmin} is minimum absolute temperature during the 24-hour period (K). During the daytime when the sun is more than 15° above the horizon, f_{cd} is calculated as:

$$f_{cd} = 1.35 \frac{R_s}{R_{s0}} - 0.35 \quad (\text{A.11})$$

Where; R_s/R_{s0} is relative solar radiation (limited to $0.3 \leq R_s/R_{s0} \leq 1.0$), R_s is measured or calculated solar radiation ($\text{MJ m}^{-2} \text{h}^{-1}$), R_{s0} is calculated clear-sky radiation ($\text{MJ m}^{-2} \text{h}^{-1}$).

For periods less than $\sim 17^\circ$ or 0.3 radians, f_{cd} is calculated:

$$f_{cd} = f_{cd \beta > 0.3} \quad (\text{A.12})$$

Where; $f_{cd \beta > 0.3}$ is cloudiness function for time period prior to when sun angle β (in the afternoon or evening) falls below 0.3 radians (dimensionless).

$$R_{so} = (0.75 + 2 * 10^{-5}z)R_a \quad (\text{A.13})$$

Where; R_{so} is clear-sky solar radiation ($\text{MJ m}^{-2} \text{h}^{-1}$), z is station elevation above sea level in (m), R_a is extraterrestrial radiation ($\text{MJ m}^{-2} \text{h}^{-1}$).

$$R_a = \frac{12}{\pi} G_{sc} d_r [(\omega_2 - \omega_1) \sin(\varphi) \sin(\delta) + \cos(\varphi) \cos(\delta) (\sin(\omega_2) - \sin(\omega_1))] \quad (\text{A.14})$$

Where; R_a is extraterrestrial radiation ($\text{MJ m}^{-2} \text{h}^{-1}$), G_{sc} is solar constant ($4.92 \text{ MJ m}^{-2} \text{h}^{-1}$), d_r is inverse relative distance factor (squared) for the earth-sun (unitless), ω_1 is solar time angle at beginning of period (radians), ω_2 is solar time angle at end of period (radians), φ is latitude (radians), positive for the Northern Hemisphere and negative for the Southern Hemisphere, δ is solar declination (radians).

$$d_r = 1 + 0.033 \cos\left(\frac{2\pi}{365}J\right) \quad (\text{A.15})$$

$$\delta = 0.409 \sin\left(\frac{2\pi}{365}J - 1.39\right) \quad (\text{A.16})$$

Where; J is number of the day in the year between 1 (January 1st) and 365 or 366 (December 31st).

Soil heat flux density is positive when the soil is warming and it is negative when the soil is cooling. Assuming a constant soil heat capacity of $2.1 \text{ MJ m}^{-3} \text{ }^\circ\text{C}^{-1}$ an appropriate soil depth, soil heat flux density:

$$G_{day} = 0 \quad (\text{A.17})$$

$$G_{month,i} = 0.07(T_{month,i+1} - T_{month,i-1}) \quad (\text{A.18})$$

For the standardized short reference ET_{os} :

$$G_{hr\ daytime} = 0.1R_n \quad (\text{A.19})$$

$$G_{hr\ nighttime} = 0.5R_n \quad (\text{A.20})$$

Where; both G and R_n in same units ($\text{MJ m}^{-2} \text{h}^{-1}$) for hourly or shorter time periods.

For the standardized tall reference ET_{rs} :

$$G_{hr\ daytime} = 0.04R_n \quad (\text{A.21})$$

$$G_{hr\ nighttime} = 0.2R_n \quad (\text{A.22})$$

For daily periods,

$$G_{day} = 0 \quad (\text{A.23})$$

APPENDIX B

Below is listed the steps that were followed for lysimeter calculations. All calculations were made in Excel 2013.

Crop canopy heights (h_c) were taken from remote sensing calculations that were calculated differently for east and west part of the research area.

$$z_{om} = 0.123 \times h_c \quad (\text{B.1})$$

$$z_{oh} = 0.1 \times z_{om} \quad (\text{B.2})$$

$$d = 0.67 \times h_c \quad (\text{B.3})$$

Where h_c is the crop height (m); z_{om} is the roughness length for the momentum transfer (m); z_{oh} is the roughness length for the heat transfer (m); and d is the zero plane displacement (m).

Friction velocity (u_*) was calculated for neutral atmospheric conditions.

$$u_* = \frac{Uk}{\ln\left(\frac{z_m - d}{z_{om}}\right)} \quad (\text{B.4})$$

Where u_* is the friction velocity (m s^{-1}); z_m is the height (m) from the ground at which the wind speed and air temperature were measured that was 2m; u is the horizontal wind speed (m s^{-1}); and k is the von Karman constant (0.41).

Then, surface aerodynamic resistance (r_{ah}) was calculated for neutral conditions:

$$r_{ah} = \frac{\ln\left(\frac{z - d}{z_{om}}\right) \ln\left(\frac{z - d}{z_{oh}}\right)}{uk^2} \quad (\text{B.5})$$

Where r_{ah} is the surface aerodynamic resistance (s m^{-1}).

Surface aerodynamic temperature T_o was calculated with SAT model;

$$T_o = 0.5T_s + 0.5T_a + 0.15r_{ah} - 1.4 \quad (\text{B.6})$$

Where T_o is the surface aerodynamic temperature ($^{\circ}\text{C}$); T_s is the surface temperature ($^{\circ}\text{C}$); T_a is the air temperature ($^{\circ}\text{C}$).

The iteration process was applied to calculate the sensible heat flux (H):

$$H = \frac{\rho_a C_{pa} (T_o - T_a)}{r_{ah}} \quad (\text{B.7})$$

Where H is the sensible heat flux (W m^{-2}); ρ_a is the air density (kg m^{-3}); C_{pa} is the specific heat of dry air ($1005 \text{ J kg}^{-1} \text{ K}^{-1}$).

Monin-Obukhov stability lengths scale (m) was calculated as:

$$L_{M_o} = \frac{-u_*^3 T_a \rho_a C_{pa}}{gkH} \quad (\text{B.8})$$

Where L_{M_o} is the Monin-Obukhov stability lengths scale (m); T_a is the surface air temperature (K); g is the gravity acceleration (9.81 m s^{-2}).

Based on stable ($L_{M_o} > 0$) and unstable ($L_{M_o} < 0$) atmospheric conditions, two different ways were followed.

For unstable ($L_{M_o} < 0$) atmospheric conditions;

$$\psi_h \left(\frac{z-d}{L} \right) = 2 \ln \left(\frac{1+x^2}{2} \right) \quad (\text{B.9})$$

$$\psi_m \left(\frac{z-d}{L} \right) = 2 \ln \left(\frac{1+x}{2} \right) + \ln \left(\frac{1+x^2}{2} \right) - 2 \text{atan}(x) + \frac{\pi}{2} \quad (\text{B.10})$$

$$x = 1 - \left(16 \left(\frac{z-d}{L_{M_O}} \right) \right)^{0.25} \quad (\text{B.11})$$

Where ψ_h is the stability correction factor for the atmospheric heat transfer; ψ_m is the stability correction factor for the momentum transfer;

For stable atmospheric conditions ($L_{M_O} > 0$):

$$\psi_m \left(\frac{z-d}{L} \right) = \psi_h \left(\frac{z-d}{L} \right) = -5 \left(\frac{z-d}{L} \right) \quad (\text{B.12})$$

Friction velocity was corrected for atmospheric conditions by using the Monin-Obukhov similarity theory:

$$u_* = \frac{uk}{\ln \left(\frac{z-d}{z_{om}} \right) - \psi_m \left(\frac{z-d}{L} \right) + \psi_m \left(\frac{z_{om}}{L} \right)} \quad (\text{B.13})$$

Then, surface aerodynamic resistance was calculated as:

$$r_{ah} = \frac{\ln \left(\frac{z-d}{z_{oh}} \right) - \psi_h \left(\frac{z-d}{L} \right) + \psi_h \left(\frac{z_{oh}}{L} \right)}{u_* k} \quad (\text{B.14})$$

Net radiation (R_n) was calculated with the incoming short wave radiation that was measured in the weather station located near the research area and surface albedo values that were computed with remote sensing:

$$R_n = (1 - \alpha)R_s + (\varepsilon_a \sigma T_a^4) - (\varepsilon_s \sigma T_s^4) \quad (\text{B.15})$$

Where R_n is net radiation (W m^{-2}); α is the surface albedo; R_s is the incoming shortwave radiation (W m^{-2}); ε_a is the emissivity of air; ε_s is the surface emissivity; σ is the Stefan Boltzmann constant ($5.67 \text{ E-8 W m}^{-2} \text{ K}^{-4}$); T_a is the air temperature (K); and T_s is the surface temperature (K).

Soil heat flux was calculated with the net radiation and LAI that were estimated with remote sensing calculations using:

$$G = R_n(0.3324 - 0.024LAI)(0.8155 - 0.3032 LN(LAI)) \quad (B.16)$$

Where G is the soil heat flux ($W m^{-2}$); R_n is the net radiation ($W m^{-2}$); and LAI is the Leaf Area Index ($m^2 m^{-2}$).

Finally, latent heat flux was calculated as a residual of net radiation, soil heat flux, and sensible heat flux:

$$LE = R_n - G - H \quad (B.17)$$

Where LE is the latent heat flux ($W m^{-2}$); R_n is the net radiation ($W m^{-2}$); G is the soil heat flux ($W m^{-2}$); and H is the sensible heat flux ($W m^{-2}$).

Instantaneous LE was converted to hourly and daily ET value:

$$\lambda = 2.501 - 0.00236T_a \quad (B.18)$$

$$ET = \frac{t \times LE}{\lambda \times \rho_w} \quad (B.19)$$

Where λ is the latent heat of vaporization ($MJ kg^{-1}$); T_a is the air temperature ($^{\circ}C$); t is the time constant (3,600 seconds for the computation of one hour); and ρ_w is the density of water ($1,000 kg m^{-3}$).

APPENDIX C

The research area was separated into four parts by using editor and clipping-data management tools then raster calculator tool was used for each calculation steps that was given in the below. All calculations were done by using model builder in ArcGIS 10.1.

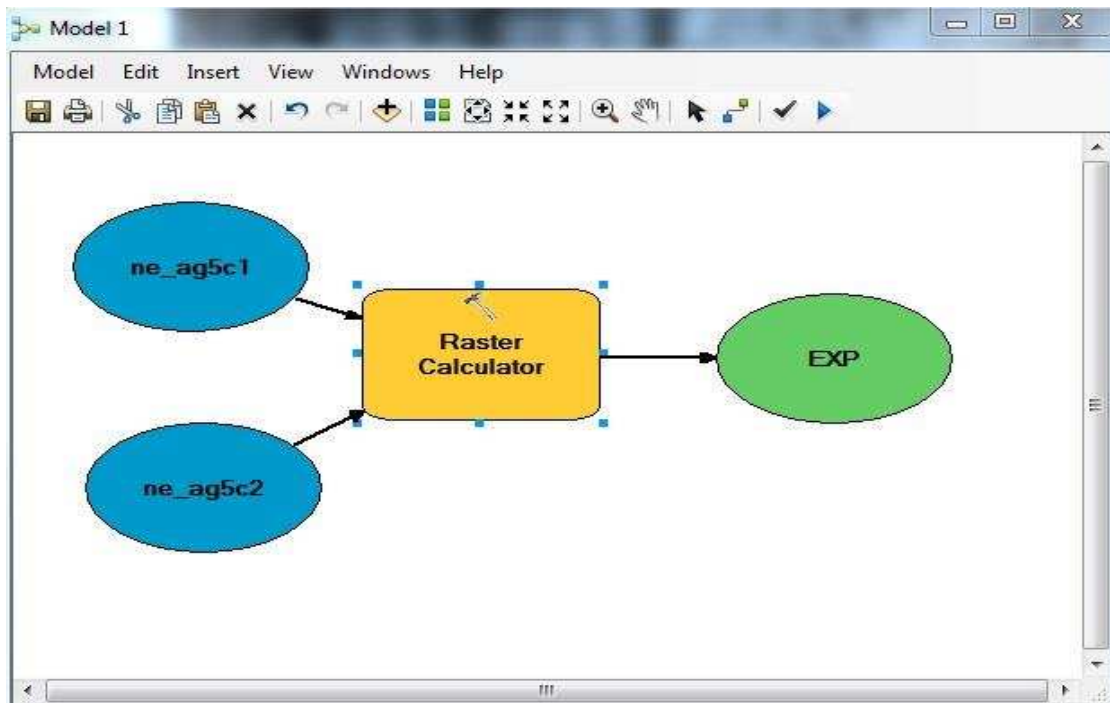


Figure B.1. Basic appearance of raster calculator.

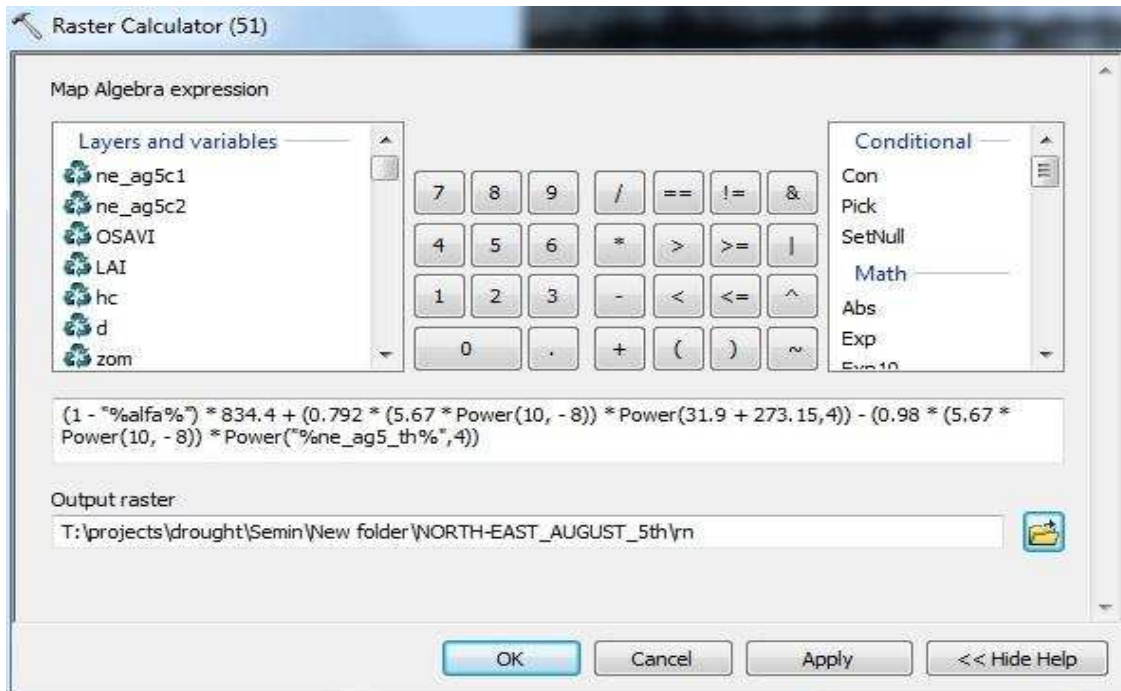


Figure B.2. Coding in raster calculator.

Below is given the calculation steps that were used in ArcGIS 10.0 model builder for the North-East part of the August 5th;

OSAVI (Optimized Soil Adjusted Vegetation Index):

$$(1.16 * ("%ne_ag5c1%" - "%ne_ag5c2%")) / (0.16 + "%ne_ag5c1%" + "%ne_ag5c2%")$$

LAI (Leaf Area Index, m²/m²):

$$0.263 * \text{Exp}(3.83 * "%OSAVI%")$$

hc_{east} (the height of the vegetation in the east side, m):

$$0.163784 * "%LAI%" + 0.195938$$

hc_{west} (the height of the vegetation in the west side, m):

$$0.052221 * "%LAI%" + 0.457288$$

d (zero plane displacement, m):

$$0.67 * \%hc\%$$

Z_{om} (roughness length for momentum transfer, m):

$$0.123 * \%hc\%$$

Z_{oh} (roughness length for heat transfer, m):

$$0.1 * \%zom\%$$

r_{ah} (surface aerodynamic resistance, s/m) for neutral atmospheric conditions:

$$(\ln((2 - \%d\%) / \%zom\%) * \ln((2 - \%d\%) / \%zoh\%)) / (2.4 * \text{Power}(0.41,2))$$

T_{aero} (aerodynamic temperature, °C):

$$0.5 * (\%ne_ag5_th\% - 273.15) + 0.5 * 31.9 + 0.15 * \%rah\% - 1.4$$

H (sensible heat flux, W/m²):

$$(1.0175 * 1005 * (\%To\% - 31.9)) / \%rah\%$$

u* (friction velocity, m/s) for neutral atmospheric conditions:

$$(2.4 * 0.41) / (\ln((2 - \%d\%) / \%zom\%))$$

L_{M o} (Monin-Obukhov stability length scale, m):

$$(- \text{Power}(\%ustar\%,3) * (31.9 + 273.15) * 1.0175 * 1005) / (9.81 * 0.41 * \%H\%)$$

x (z):

$$\text{Power}(1 - 16 * (2 - \%d\%) / \%Lmo\%, 0.25)$$

x (zoh):

$$\text{Power}(1 - 16 * \%zoh\% / \%Lmo\%, 0.25)$$

x (zom):

$$\text{Power}(1 - 16 * \%zom\% / \%Lmo\%, 0.25)$$

$\psi_h(z)$:

$$2 * \text{Ln}((1 + \text{Power}(\%x(z)\%, 2)) / 2)$$

$\psi_h(zoh)$:

$$2 * \text{Ln}((1 + \text{Power}(\%x(zoh)\%, 2)) / 2)$$

$\psi_m(z)$:

$$2 * \text{Ln}((1 + \%x(z)\%) / 2) + \text{Ln}((1 + \text{Power}(\%x(z)\%, 2)) / 2) - 2 * \text{ATan}(\%x(z)\%) + 3.1416 / 2$$

$\psi_m(zom)$:

$$2 * \text{Ln}((1 + \%x(zom)\%) / 2) + \text{Ln}((1 + \text{Power}(\%x(zom)\%, 2)) / 2) - 2 * \text{ATan}(\%x(zom)\%) + 3.1416 / 2$$

u* (friction velocity, m/s):

$$(2.4 * 0.41) / (\text{Ln}((2 - \%d\%) / \%zom\%) - \%wm(z)\% + \%wm(zom)\%)$$

rah (surface aerodynamic resistance, s/m):

$$\frac{\ln\left(\frac{2 - \%d\%}{\%zoh\%} - \%wh(z)\% + \%w(zoh)\%\right)}{(\%ustr_2\% * 0.41)}$$

alfa (surface albedo):

$$0.512 * \%ne_ag5c2\% + 0.418 * \%ne_ag5c1\%$$

Rn (net radiation, W/m²):

$$(1 - \%alfa\%) * 834.4 + (0.792 * (5.67 * \text{Power}(10, -8)) * \text{Power}(31.9 + 273.15,4)) - (0.98 * (5.67 * \text{Power}(10, -8)) * \text{Power}(\%ne_ag5_th\%,4))$$

G (soil heat flux, W/m²):

$$(((0.3324 + (-0.024 * \%LAI\%)) * (0.8155 + (-0.3032 * \ln(\%LAI\%)))) * \%Rn\%)$$

LE (latent heat flux, W/m²):

$$\%Rn\% - \%G\% - \%H_4\%$$

ET (evapotranspiration, mm/h):

$$(3600 * \%le\% * \text{Power}(10,3)) / (2.4361 * \text{Power}(10,9))$$

APPENDIX D

First reference ET values were calculated by using REF-ET calculator.

Table D.1. Reference ET values that were calculated with REF-ET calculator

Etr (mm/d)	Eto (mm/d)	Etr(mm/h)	Eto(mm/h)
24.10	18.60	1.00417	0.77500
18.10	14.40	0.75417	0.60000
18.80	15.80	0.78333	0.65833
20.00	16.90	0.83333	0.70417
20.40	17.80	0.85000	0.74167
17.30	15.00	0.72083	0.62500

For east part of the research area;

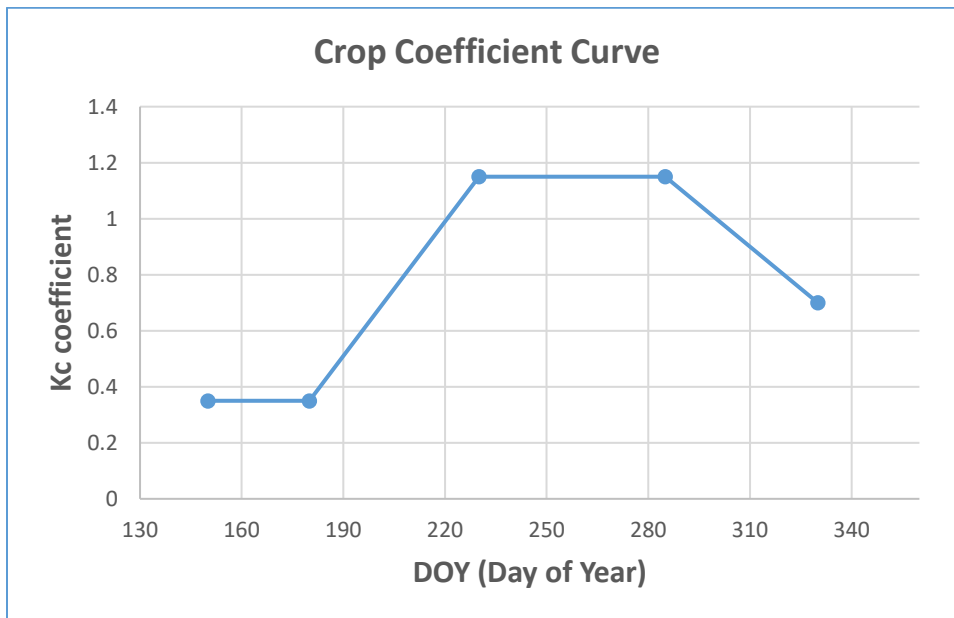


Figure D.1. Crop coefficient curve for east part of the research area

Table D.2. Calculated potential ET values based on Kc and reference ET values for east part of the research area

DOY	Kc	Eto(mm/h)	Etp (mm/h)
178	0.35	0.775	0.271
194	0.57	0.600	0.344
202	0.70	0.658	0.462
210	0.83	0.704	0.584
218	0.96	0.742	0.711
226	1.09	0.625	0.679

For west part of the research area;

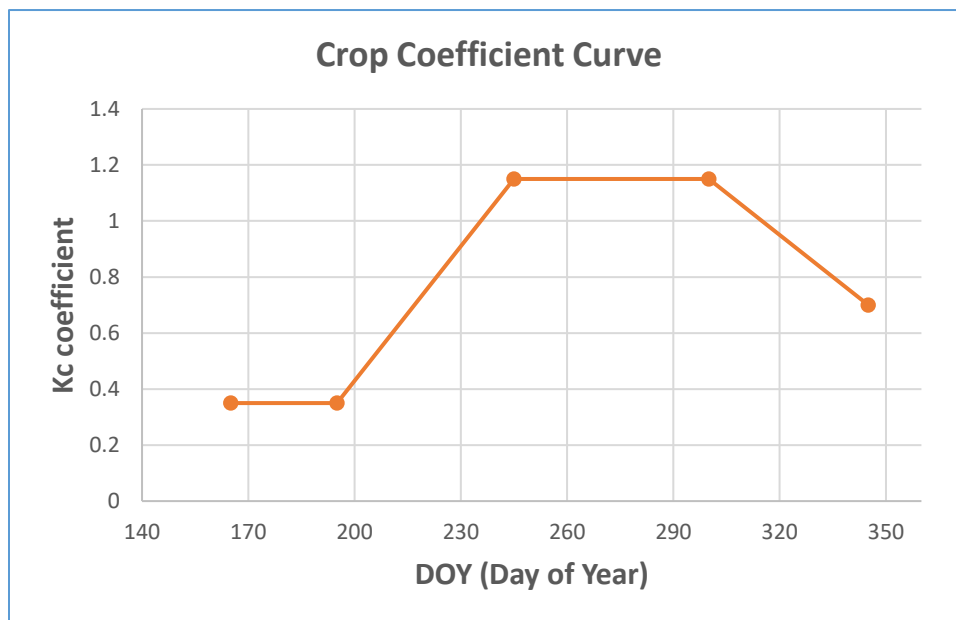


Figure D.2. Crop coefficient curve for east part of the research area

Table D.3. Calculated potential ET values based on Kc and reference ET for west part of the research area

DOY	Kc	Eto(mm/h)	Etp (mm/h)
178	0.35	0.775	0.271
194	0.35	0.600	0.210
202	0.462	0.658	0.304
210	0.59	0.704	0.415
218	0.718	0.742	0.533
226	0.846	0.625	0.529